

# Quantifying riming from airborne data during HALO-(AC)<sup>3</sup>

Nina Maherndl<sup>1</sup>, Manuel Moser<sup>2,3</sup>, Johannes Lucke<sup>3,4</sup>, Mario Mech<sup>5</sup>, Nils Risse<sup>5</sup>, Imke Schirmacher<sup>5</sup>, and Maximilian Maahn<sup>1</sup>

<sup>1</sup>Leipzig Institute of Meteorology (LIM), Leipzig University, Leipzig, Germany

<sup>2</sup>Institute for Physics of the Atmosphere, Johannes Gutenberg University, Mainz, Germany

<sup>3</sup>Institute for Physics of the Atmosphere, German Aerospace Center (DLR), Wessling, Germany

<sup>4</sup>Faculty of Aerospace Engineering, Delft University of Technology, Delft 2629, the Netherlands

<sup>5</sup>Institute for Geophysics and Meteorology, University of Cologne, Cologne, Germany

**Correspondence:** Nina Maherndl (nina.maherndl@uni-leipzig.de)

**Abstract.** Riming is a key precipitation formation process in mixed-phase clouds by efficiently converting cloud liquid to ice water. Here, we present two methods to quantify riming of ice particles from airborne observations with the normalized rime mass, which is the ratio of rime mass to the mass of a size-equivalent spherical graupel particle. We use data obtained during the HALO-(AC)<sup>3</sup> aircraft campaign, where two aircraft were collecting spatially and temporally closely collocated radar and in situ measurements over the Fram Strait west of Svalbard in spring 2022. The first method is based on an inverse Optimal Estimation algorithm to retrieve the normalized rime mass from a closure between cloud radar and in situ measurements during these collocated flight segments ("combined method"). The second method relies on in situ observations only, by relating the normalized rime mass to optical particle shape measurements ("in situ method"). We find good agreement between both methods during collocated flight segments with median normalized rime masses of 0.024 and 0.021 (mean values of 0.035 and 0.033) for combined and in situ method, respectively. Assuming particles with a normalized rime mass smaller 0.01 to be unrimed, we obtain average rimed fractions of 88 % and 87 % over all collocated flight segments, respectively. Although in situ measurement volumes are in the range of a few cm<sup>3</sup> and therefore much smaller than the radar volume (about 45 m footprint diameter at an altitude of 500 m above ground; with a vertical resolution of 5 m), we assume they are representative of the radar volume. When this assumption is not met due to less homogeneous conditions, discrepancies between the two methods result. We show the performance of the methods in a case study of a collocated segment in cold air outbreak conditions and compare normalized rime mass results with meteorological and cloud parameters. We find that higher normalized rime masses correlate with streaks of higher radar reflectivity. The methods presented improve our ability to quantify riming from aircraft observations.

## 1 Introduction

Mixed-phase clouds (MPC) are a crucial part of the Arctic climate system. Observations have shown that MPC occur about 40 % of the time (e.g., at Barrow, Alaska or Ny-Alesund, Svalbard; Shupe, 2011; Gierens et al., 2020), can persist up to several days (Zuidema et al., 2005), and can span hundreds of kilometers by forming organized cloud streets during cold air outbreaks (Müller et al., 1999). MPC play a critical role in the Arctic hydrological cycle and radiation budget, having on average a positive

surface radiative forcing (Shupe and Intrieri, 2004; Kay and L'Ecuyer, 2013). However, the role of MPC in a rapidly warming  
25 Arctic ("Arctic Amplification"), where the mean near-surface air temperature has increased nearly four times more than the  
global mean during the last four decades (Rantanen et al., 2022), is not fully understood yet. It is unclear, whether changes in  
MPC properties or frequency of occurrence will accelerate or decelerate Arctic amplification (Wendisch et al., 2023).

MPC properties are in part determined by microphysical processes. Supercooled liquid water droplets (SLW) can coexist  
with ice particles in MPC between 0 °C and about -38 °C; at colder temperatures, homogeneous freezing occurs. Typically,  
30 MPC are composed of a single or multiple stratiform layers of SLW near the cloud top and ice particles within and beneath the  
SLW layers (Shupe et al., 2006). While this composition is thermodynamically unstable, long MPC life times are driven by  
a combination of various processes and feedback mechanisms that are poorly understood (Morrison et al., 2012). The repre-  
sentation of these processes poses a major source of uncertainty in numerical weather forecast and climate models (Morrison  
et al., 2020).

35 One important ice growth process, besides aggregation and depositional growth, common in MPC is riming. Riming occurs,  
when SLW comes into contact with ice particles, freezing onto them almost instantly. Typically, riming leads to denser, more  
spherical ice particles with increased mass, size, and fall velocity (Heymsfield, 1982; Erfani and Mitchell, 2017; Seifert et al.,  
2019). Due to its efficiency in converting SLW, riming is a key process for ice growth and subsequent precipitation formation.  
Moisseev et al. (2017) showed that in Hyytiälä (Finland) riming was responsible for 5 % to 40 % of snowfall mass during  
40 winter 2014/2015 whereas Harimaya and Sato (1989) found riming proportions above 50 % for snowfall in a Japanese seaside  
area in 1987. Nonetheless, riming is often neglected in studies of Arctic MPC (Avramov et al., 2011; Yang et al., 2013; Oue  
et al., 2016), especially in cases with low liquid water paths (LWP). Fitch and Garrett (2022) showed in a recent study that  
riming is very common in Arctic low-level MPC, also in cases of LWP less than 50 gm<sup>-2</sup>. Only 34 % of precipitating particles  
observed at Oliktok Point, Alaska showed negligible amounts of riming. They proposed that riming enhancement can occur in  
45 regions with updrafts so that particles are exposed to SLW for a longer time span before falling out.

Riming has been studied in situ by airborne or ground-based measurements. Individual ice crystals or snowflakes that are  
observed manually (Harimaya and Sato, 1989; Mosimann et al., 1994) or by optical probes (Praz et al., 2017; Waitz et al.,  
2022) are often qualitatively classified. Mosimann (1995) was the first to quantify the degree of snow crystal riming using  
radar Doppler velocity measurements. They defined the riming degree on a scale from 0 to 5, where 0 means unrimed, 3 means  
50 heavily rimed and 5 means graupel. Mason et al. (2018) retrieved a "density factor" as a proxy for riming from dual-frequency  
radar Doppler velocity measurements. Kneifel and Moisseev (2020) presented long-term statistics of the rime mass fraction  
(FR), the ratio of rime mass and snow particle mass, also obtained by Doppler velocity measurements, whereas Vogl et al.  
(2022) showed that FR can be predicted by an artificial neural network from radar reflectivity  $Z_e$  and skewness measurements.  
Previous studies have shown that collocating radar signals and in situ cloud data can be used to create, improve and validate  
55 microphysical cloud retrievals (Tian et al., 2016; Trömel et al., 2021; Blanke et al., 2023).

In the Arctic, there are only few observations of riming given the difficulty of 1) obtaining (quantitative) measurements of  
riming in general and 2) performing cloud measurements in remote regions. Airborne campaigns offer unique opportunities  
of measuring in regions that are otherwise inaccessible. Waitz et al. (2022) showed observations of ice particles by optical

probes collected during ACLOUD (Arctic CLOUD Observations Using airborne measurements during polar Day, May/June 2017 based in Svalbard, Wendisch et al., 2019). Images of ice particles are observed manually and qualitatively classified as "unrimed", "slightly rimed", "moderately rimed", "heavily rimed", and "graupel". Nguyen et al. (2022) presented coincident triple frequency radar and in situ observation obtained during the RadSnowExp (Radiation Snow Experiment, fall 2018 based in Iqaluit, Canada; Wolde et al., 2019). They show close relationships between the triple-frequency signatures and in situ derived effective ice particle bulk density, which functions as a proxy for riming. Further, they compare to a machine learning ice particle habit classification that includes "rimed" categories. While both Waitz et al. (2022) and Nguyen et al. (2022) show the common occurrence of riming in Arctic MPC and the high value of aircraft observation to study riming, neither method can quantify the fraction riming contributes to particles' mass.

In this study, we present two methods to quantify riming from airborne measurements and apply them to data collected during the aircraft campaign Arctic Air Mass Transformations during Warm Air Intrusions and Marine Cold Air Outbreaks (HALO-(AC)<sup>3</sup>). HALO-(AC)<sup>3</sup> took place in March/April 2022 with the main objective to study Arctic air mass transformations and conduct collocated measurements with up to three aircraft. We focus on (collocated) remote sensing and in situ measurements obtained with the research aircraft Polar 5 and Polar 6, respectively. Both aircraft were based in Svalbard and measurements were mainly collected over the open ocean and in the marginal sea ice zone (MIZ), the transition zone between open ocean and closed sea ice, west of Svalbard. We use the normalized rime mass  $M$  (Seifert et al., 2019), the ratio of rime mass to the mass of an equally large graupel particle, to quantify riming. The first method is based on an Optimal Estimation algorithm to obtain  $M$  from a closure between cloud radar and in situ measurements during collocated flight segments ("combined method", see Sect. 3.1). We find  $M$  by matching measured radar reflectivities  $Z_e$  with simulated  $Z_e$  obtained from observed in situ particle number concentrations. The second method derives  $M$  from in situ measured particle shape ("in situ method", see Sect. 3.2). We compare results for  $M$  obtained with both methods for all collocated flight segments (Sect. 4.1). We then present a case study of a collocated flight segment from 01 April during cold air outbreak conditions (Sect. 4.2) to show the performance of the two methods. Further, we investigate the relation of  $M$  to meteorological and cloud parameters such as temperature, liquid water content (LWC), total water content (TWC), LWP, and in-cloud location (Sect. 4.3). Last, we analyze all in situ data and evaluate how representative the collocated segments are for the whole campaign (Sect. 4.4).

## 2 Data

### 2.1 The HALO-(AC)<sup>3</sup> airborne campaign

In this study, radar and in situ data from the HALO-(AC)<sup>3</sup> campaign (Wendisch, M. et al., 2023) are analyzed. During the campaign organized by the Transregional Collaborative Research Centre TR 172 (AC)<sup>3</sup>, three research aircraft were employed to study the Arctic atmosphere. The main objectives of the campaign included investigating warm air intrusions into the Arctic as well as marine cold air outbreaks (MCAO) and collecting collocated measurements with up to three aircraft (Wendisch, M. et al., 2023). The synoptic situation during the campaign is described in Walbröl et al. (2023). The instrumentation on board the Polar aircraft is similar to the one used during the Airborne measurements of radiative and turbulent FLUXes of energy

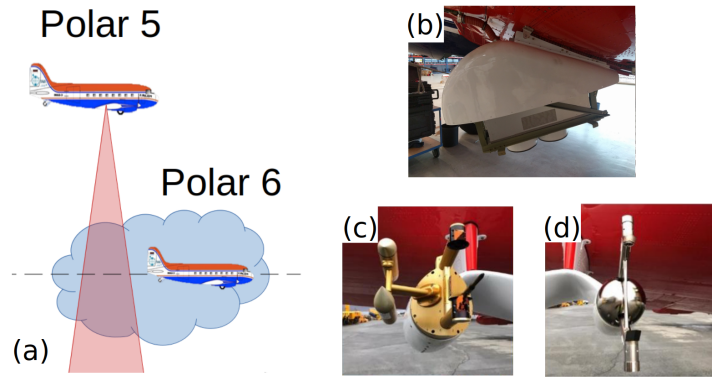


**Figure 1.** (a) Concept of collocation: while a radar onboard Polar 5 is measuring the cloud from above, cloud probes onboard Polar 6 simultaneously collect in situ samples at (almost) the same location inside the cloud. (b) MiRAC-A on Polar 5 in its belly pot and the wing-mounted cloud probes (c) Cloud Droplet Probe (CDP), Cloud Imaging Probe (CIP) and (d) Precipitation Imaging Probe (PIP) on Polar 6.

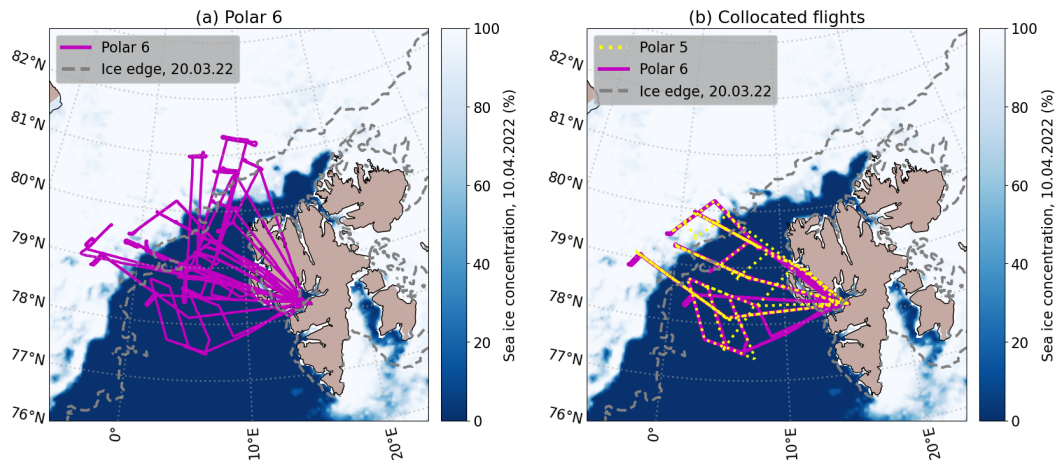


**Figure 2.** Flight tracks of (a) all Polar 6 flights (in situ) conducted during HALO-(AC)<sup>3</sup> and (b) flights with collocated Polar 5 (remote sensing) and Polar 6 segments. The sea ice concentration (SIC) derived from the Advanced Microwave Scanning Radiometer 2 (AMSR2) onboard the GCOM-W1 satellite on 10 April (at campaign end) is shaded in blue; The ice edge (15 % SIC) on 20 March (at campaign start) is shown in light gray.

and momentum in the Arctic boundary layer (AFLUX) and Multidisciplinary drifting Observatory for the Study of Arctic Climate – Airborne observations in the Central Arctic (MOSAIC-ACA) campaigns described in Mech et al. (2022a). During the majority of flights analyzed in this study, north and northeasterly wind transported cold air masses from the central Arctic to the main measurement area in the Fram Strait.

We focus on data collected by Polar 5 and Polar 6, two Basler BT-67 aircraft operated by the Alfred Wegener Institute, Helmholtz Centre for Polar and Marine Research (AWI; Wesche et al., 2016). A total of 11 flights with Polar 5 and 13 with

Polar 6 were conducted in March and April 2022 during HALO-(AC)<sup>3</sup> in the vicinity of Svalbard. Closely collocated and nearly coincident measurements were obtained with the W-band cloud radar component of the Microwave Radar/radiometer for Arctic Clouds (MiRAC-A, Mech et al., 2019) on board of Polar 5 and a variety of in situ cloud probes mounted under the wings of Polar 6 (Mech et al., 2022a). Figure 1 (a) shows a conceptional sketch of how collocation was achieved: while Polar 6 was flying low and in-cloud, Polar 5 was following in close proximity on the same track above. The slight off-set between the two planes was necessary so that dropsondes could be released safely from Polar 5.

Figure 2 shows (a) all flight tracks of Polar 6 and (b) flight tracks of both aircraft for flights with collocated segments. The overlapping lines show close spatial collocation. The sea ice concentration (SIC) at campaign beginning and end indicate the variable sea ice conditions. All 13 Polar 6 flights result in over 60 hours of flight time and about 32 hours of cloud particle measurements. 31 % of the total flight time during the flights shown in Fig. 2 (b) was conducted "collocated", which we define as both aircraft having a maximum horizontal distance of 5 km within a 5 min time window. From a total of about 11.8 hours of collocated flight time, 4.6 hours are collocated cloud measurements (this corresponds to a distance of approximately 1300 km assuming a typical speed of 80 ms<sup>-1</sup>). The analyzed data covers a temperature range of -31 to -1 °C and an altitude range of in cloud measurements from close to the ground to 1760 m.

## 2.2 In situ cloud probes

During HALO-(AC)<sup>3</sup>, a variety of in situ cloud data was collected. This study uses microphysical cloud data collected from three different cloud instruments, the Cloud Droplet Probe (CDP; Lance et al., 2010; Wendisch et al., 1996), the Cloud Imaging Probe (CIP; Baumgardner et al., 2011) and the Precipitation Imaging Probe (PIP; Baumgardner et al., 2011). All three probes were installed under the wings of Polar 6 (Fig. 1) and operated by the German Aerospace Center (DLR). The CDP is a forward-scattering optical spectrometer. The instrument measures cloud particles in the size range 2.8 to 50 μm by the intensity of forward scattered laser light underlying Mie theory. Larger cloud particles are measured via Optical Array Probes (OAP). Here, two-dimensional shadow images of the cloud particles are recorded as the particles pass through the instrument's sampling area. The collected data by the CIP and PIP differ in pixel resolution. Both instruments consist of a 64 diode array with the CIP covering a size range from 15 μm to 960 μm (15 μm resolution) and the PIP covering from 103 μm to 6.4 mm (103 μm resolution). By combining CDP, CIP and PIP, a continuous particle size distribution is derived including all hydrometeors from 2.8 to 6400 μm. The same processing methods of the OAP data is applied as used for the AFLUX and MOSAiC-ACA campaigns (Moser and Voigt, 2022; Moser et al., 2022). The operating principle of the respective instruments, processing, uncertainties and applied corrections is described in detail by Moser et al. (2023) and Mech et al. (2022a).

Liquid water content (LWC) and total water content (TWC) were measured with a Nevzorov probe (Korolev et al., 1998). The probe was operated with a new sensor head, which featured an LWC sensor and two TWC cones with diameters of 8 and 12 mm (Lucke et al., 2022). The Nevzorov probe contains sensing elements which are regulated to provide a constant temperature, (110°C during the HALO-(AC)<sup>3</sup> campaign). Droplets and ice particles momentarily cool the sensing elements when they impinge. In consequence, the sensors draw more power as they heat and evaporate impinging water in order to maintain their temperature, which can be used to estimate bulk LWC and bulk TWC. The measurement range of the Nevzorov

probe extends from approximately 0.01 to 3.0 gm<sup>-3</sup>. Uncertainties of the Nevzorov depend very much on the atmospheric conditions that are present (Lucke et al., 2022). Nevzorov probe measurements during HALO-(AC)<sup>3</sup> are only available for flights in April due to technical difficulties in March. Air temperature was measured with a Pt100 mounted in a Rosemount-  
135 housing at the noseboom of Polar 6. The measurements were corrected for adiabatic heating in the housing.

With the collected data, we are unable to distinguish between larger liquid droplets and small solid ice particles due to low resolution images consisting of only a few pixels. We therefore assume all cloud particles with sizes larger 50 μm to be ice crystals and all cloud particles with sizes smaller 50 μm to be liquid droplets similar to Moser et al. (2023). For the majority of low-level Arctic MPC, this is appropriate to assume (McFarquhar et al., 2007; Korolev et al., 2017). This assumption is based  
140 on the good agreement between Nevzorov probe LWC and LWC calculated from the PSD assuming particles smaller 50 μm to be liquid droplets where both measurements are available ( $R^2 = 0.83$ ; Nevzorov and PSD LWC sum up to 973 and 983 gm<sup>-3</sup>, respectively, and lie within 1 % of each other). Additionally, we do not expect this assumption will lead to significant biases due to radar reflectivities (that we simulate from in situ PSDs) being dominated by large particles.

### 2.3 Airborne remote sensing instruments

145 The Microwave Radar/radiometer for Arctic Clouds (MiRAC; Mech et al., 2019) was designed for operation on board the research aircraft Polar 5. During HALO-(AC)<sup>3</sup> the active radar component (MiRAC-A) was operated on board of Polar 5 in the same constellation as during MOSAiC-ACA. MiRAC-A is a 94 GHz frequency-modulated continuous wave (FMCW) radar, which was mounted with an inclination angle of 25° backward in a belly pod under Polar 5. The radar measurements have been quality controlled and corrected for surface clutter, mounting of the instrument, and aircraft attitude (Mech et al., 2019).  
150 This results in geo-referenced, regularly gridded data with a vertical resolution of 5 m (with reliable measurements starting 150 m above ground level due to ground clutter effects and 200 m distance from the aircraft for full overlap). Mech et al. (2019) estimate the accuracy of the radar reflectivity  $Z_e$  calibration to be 0.5 dBZ (neglecting attenuation). Because Doppler velocity measurements are biased by the aircraft motion, only  $Z_e$  measurements are used in this study.

The MiRAC-A radar is also equipped with a horizontally-polarized 89 GHz passive channel using the same antenna as the  
155 radar. The brightness temperature ( $T_B$ ) is also measured under a tilted angle of 25° backwards to nadir. From this observations, the liquid water path (LWP) is estimated over open ocean only with a temporal resolution of 1 s as described in Ruiz-Donoso et al. (2020). The retrieval takes profiles of nearby dropsondes to calculate  $T_B$  as a function of LWP measurements from simulations with the Passive and Active Microwave radiative TRANSfer tool (PAMTRA, Mech et al., 2020).  $T_B$ (LWP) is approximated by a third-order regression. The regression is then applied in an inverse scheme to the 89 GHz  $T_B$  measurements  
160 to derive LWP. To eliminate biases in the observations, the difference between clear-sky and cloudy observations were used. Due to the variable microwave emissivity of sea ice, the LWP product is only available above open ocean.

Cloud top height (CTH) is obtained from the Airborne Mobile Aerosol Lidar for Arctic research (AMALi; Stachlewska et al., 2010), which was also operated on Polar 5. AMALi measures backscatter intensity profiles at 532 nm (polarized) and 355 nm (not polarized), from which the attenuated backscatter coefficient is calculated (Ehrlich et al., 2019). CTH is determined by  
165 searching for gradients in the backscatter coefficient.

For the present study,  $Z_e$  has been corrected for attenuation due to atmospheric gases as well as liquid hydrometeors. The two-way attenuation profile was calculated with PAMTRA. We used measurements from the closest dropsonde and the water vapor absorption model by Rosenkranz (Rosenkranz, 1998) to calculate the attenuation due to water vapor for each time step. To estimate attenuation due to liquid water, we took LWC measurements from the Nevzorov probe operated onboard Polar 6 during the temporally closest vertical cloud profile. To obtain information on the vertical structure of clouds, Polar 6 flew vertical profiles in so-called "saw-tooth patterns". These patterns were flown in addition to straight legs at constant altitudes. Saw-tooth patterns are not well suited for good quality collocated measurements with Polar 5, where straight legs are preferred. Therefore a limited number of vertical profiles are available for each flight with collocation. During each flight analyzed in this study, at least three of such "saw-tooth patterns" were collected. Whenever Nevzorov probe measurements were not available, LWC was calculated by integrating the particle size distribution (PSD) of liquid particles ( $< 50 \mu\text{m}$ ) measured with the cloud probes on board Polar 6. In both cases, LWC measurements were averaged to be on a regular vertical grid with a resolution of 10 m. Here, we neglect the distance traveled by Polar 6 during the profile, assuming LWC to be constant at each height bin. This assumption likely does not hold in reality, however, no measurements with more precise information on horizontal and vertical LWC distributions are available. Attenuation due to snowfall is assumed to be negligible compared to liquid droplets. During HALO-(AC)<sup>3</sup> we obtain a mean two-way attenuation of 0.41 dB. By comparing integrated LWC measured with the Nevzorov probe and LWC calculated from PSD during cloud profiles (if both are available) to the temporally higher resolved LWP from MiRAC-A, we estimate uncertainties of the attenuation correction to be 1 dB leading to a total uncertainty of  $Z_e$  of 1.5 dB.

#### 2.4 Collocation of radar and in situ measurements

In order to combine radar and in situ measurements, it is critical to have a temporally and spatially collocated data set. Following Chase et al. (2018) and Nguyen et al. (2022), the nearest radar data point to the in situ measurements is selected. We matched each 1 Hz Polar 5 data point with the spatially closest Polar 6 data point with a maximum horizontal distance of 5 km within a 5 min time window. Further, the radar range gate closest to the flight altitude of Polar 6 was chosen. Averaging radar reflectivity over certain height ranges close to Polar 6 did not lead to improvements. A rolling average of 30 s was applied to in situ data to obtain more robust statistics and to the radar data to make results comparable. Also, this is done to compensate for the different sampling volumes to a certain extent. While the radar footprint of a cloud in 2500 m distance is approximately 45.15 m in diameter, the cloud probes have measurement volumes in the range of a few cubic centimeters. We are aware that the assumption that the in situ measurement is representative of the entire matched radar volume is not always met and discuss possible implications of the assumption for our results in Sect. 5.

#### 2.5 Simulated rimed aggregates

In addition to the observations, we use a data set of simulated rimed aggregates to relate particle properties and riming as discussed in Maherndl et al. (2023a). The aggregation and riming model described in Leinonen et al. (2013), Leinonen and Szyrmer (2015) and Leinonen and Moisseev (2015) is used in the setting "B" (aggregation followed by riming) to generate

aggregates built from a predefined number of monomer crystals. The monomer crystal sizes are taken from an exponential size  
 200 distribution and the crystals themselves are composed of cubic volume elements with an edge length of 20  $\mu\text{m}$ . The aggregate  
 sizes range from slightly below 100  $\mu\text{m}$  to 12 mm. In this study, we only use dendrite monomer crystals, which is motivated  
 by manual inspection of the in situ images for the collocated flight segments. After aggregation, the particles are exposed to  
 a predefined amount of liquid water so that riming occurs. The frozen droplets that have rimed onto the ice particles are also  
 represented by cubic volume elements of 20  $\mu\text{m}$ .

### 205 3 Methodology

Here, we describe how we obtain quantitative measures of riming in two different ways. To quantify riming, we use the  
 normalized rime mass  $M$  (Seifert et al., 2019), which is defined as the rime mass  $m_{\text{rime}}$  divided by the mass of the size-  
 equivalent spherical graupel particle  $m_g$ , where we assume a rime density of  $\rho_{\text{rime}} = 700 \text{ kg m}^{-3}$ :

$$M = \frac{m_{\text{rime}}}{m_g} \quad (1)$$

210 where

$$m_g = \frac{\pi}{6} \rho_{\text{rime}} D_{\text{max}}^3. \quad (2)$$

The definition of  $M$  implies  $M = 0$  for unrimed particles and  $M \rightarrow 1$  for heavily rimed, spherical graupel particles. The  
 maximum dimension  $D_{\text{max}}$  is defined as the diameter of the smallest circle encompassing the cloud particle in m and is used to  
 parameterize particle sizes during the whole study (only for the in situ method, we convert  $D_{\text{max}}$  from physical units to pixel  
 215 number).

First, we present an algorithm based on Optimal Estimation (Rodgers, 2000; Maahn et al., 2020) to retrieve average  $M$  of  
 observed cloud particle populations for each time step from a closure of collocated remote sensing and in situ data ("combined  
 method"; Sect. 3.1). Second, we describe the calculation of  $M$  based on in situ measured cloud particle shape. We use a data  
 set of simulated rimed aggregates to relate particle shape to  $M$  and apply the method to in situ measurements of particle shape  
 220 ("in situ method"; Sect. 3.2).

#### 3.1 Combined method

We take advantage of collocated Polar 5 and Polar 6 flights and retrieve the average  $M$  of the observed cloud particle population  
 value for each time step from the combination of radar and in situ measurements (Fig. 3).

First,  $Z_e$  is corrected for attenuation (see Sect. 2.3), all cloud edges are removed to avoid non uniform beam filling and  
 225 Polar 5 and Polar 6 data is combined (see Sect. 2.4). PAMTRA (Mech et al., 2020) is used to simulate  $Z_e$  from the in situ  
 PSD and an initial guess for  $M$ . In principle,  $Z_e$  is a function of the mass, PSD, and scattering properties of the observed  
 particle population. If the PSD is known and particle mass and backscattering are parameterized as a function of riming,  $M$   
 can be derived from a closure of  $Z_e$  and PSD. In the retrieval radar forward operator, we use Mie scattering (Mie, 1908) for



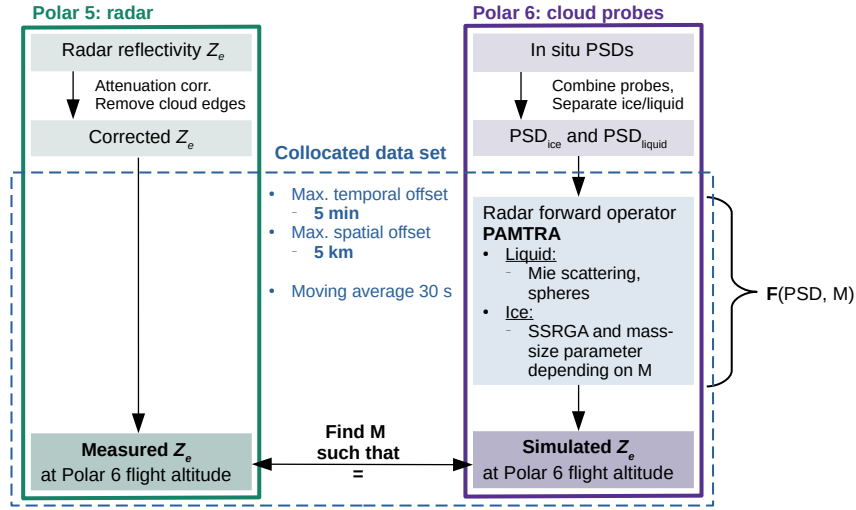


**Figure 3.** Schematic of the retrieval framework.

liquid droplets. For ice particles, we use the Self-Similar Rayleigh-Gans approximation (SSRGA; Hogan and Westbrook, 2014; Hogan et al., 2017) and calculate the required SSRGA parameters from  $M$  with the empirical relations presented in Mahernndl et al. (2023a). In addition, we consider the mass-size relation to follow a power law ( $m = a_m \cdot D_{\max}^{b_m}$ ), and take the mass-size parameters  $a_m$  and  $b_m$  for dendrites from the same study. There  $a_m$  and  $b_m$  are given for discrete  $M$ , so we interpolate  $a_m$  and  $b_m$  to obtain parameters for a continuous  $M$ . We discuss the assumption on particle shape in Appendix A.

By parameterizing scattering as well as mass-size relations only by  $M$  and assuming that the measured PSDs are representative of radar measurements, we can tweak  $M$  until measured and forward simulated radar reflectivities match within a given uncertainty range. This is done by Optimal Estimation (OE), a retrieval technique based on Bayes' theorem (Rodgers, 2000) implemented in pyOptimalEstimation (Maahn et al., 2020). OE uses a priori information  $\mathbf{x}_a$  and a Gaussian statistical model to estimate the state vector  $\mathbf{x}$  from the observation vector  $\mathbf{y}$  in an iterative scheme. Starting with  $\mathbf{x}_a$  as a first guess for  $\mathbf{x}$ , the forward model  $F(\mathbf{x})$  (i.e., PAMTRA) is used to convert state to observation space. Then, the difference between  $\mathbf{y}$  and  $F(\mathbf{x}_a)$  is used to make a next guess for the state vector  $\mathbf{x}_1$ , which requires inverting  $F(\mathbf{x})$  with the help of the Jacobian matrix  $\mathbf{K} = \partial F(\mathbf{x})/\partial \mathbf{x}$ . This scheme is repeated until the posteriori probability distribution  $P(\mathbf{x}|\mathbf{y}) = P(\mathbf{y}|\mathbf{x})/P(\mathbf{y})$  reaches a maximum resulting in the optimal  $\mathbf{x}$ . This is achieved by minimizing the cost function  $J$ :

$$J = [\mathbf{y} - F(\mathbf{x})]^T \mathbf{S}_y^{-1} [\mathbf{y} - F(\mathbf{x})] + (\mathbf{x} - \mathbf{x}_a)^T \mathbf{S}_a^{-1} (\mathbf{x} - \mathbf{x}_a) \quad (3)$$

where  $\mathbf{S}_y$  is the uncertainty of  $\mathbf{y}$  (observation covariance matrix) and  $\mathbf{S}_a$  the a-priori uncertainty (covariance matrix of  $\mathbf{x}_a$ ).  
 245 Given that our problem is unambiguous (one measurement parameter  $\mathbf{y}$  ( $Z_e$ ) and one state parameter  $\mathbf{x}$  ( $M$ )), using OE is not strictly necessary but has the advantage of providing uncertainties.

We choose  $\mathbf{x}$  to represent  $M$  in common logarithmic scale ( $x = [\log_{10}(M)]$ ) to avoid negative values. We use  $\mathbf{x}_a = -1$  (corresponding to  $M = 0.1$ ) as a-priori information and  $\mathbf{S}_a=1$  as a-priori uncertainty. We also evaluated different a-priori guesses  $\mathbf{x}_a$  and uncertainties  $\mathbf{S}_a$ , but they lead to almost identical results and are therefore not shown.  $\mathbf{y}$  are the attenuation  
 250 corrected  $Z_e$  measurements at Polar 6 flight altitude in dBZ and  $\mathbf{S}_y$  represents the corresponding measurement uncertainty of 1.5 dB. Uncertainties due to non-exact collocation between Polar 5 and 6 are neglected here. The average standard deviation of  $Z_e$  is 0.7 dB over distances of 555 m, which corresponds to the mean horizontal distance between the aircraft, and therefore smaller than the assumed uncertainty of 1.5 dB. In Sect. 4 we discuss implications of the non-exact collocation on the presented results. In Appendix B we show that the OE output captures uncertainties of the combined method with synthetic data.

### 255 3.2 In situ method

The second method exploits the fact that riming impacts ice particle shape and typically leads to more spherical particles that can be derived from in situ image properties obtained by the CIP and PIP. This method can, in principle, be applied to all Polar 6 cloud particle measurements. From the captured images, hydrometeor properties described in the following were estimated.  $D_{\max}$ , particle cross-sectional area  $A$ , and the perimeter area  $P$  are derived in the unit of pixel numbers. For the calculation of  
 260  $A$  and  $P$ , only particles that do not touch the edges of the OAP are used (Crosier et al., 2011). From  $A$  and  $P$  in the unit of pixel numbers, we calculate the complexity parameter  $\chi$ , which we define as:

$$\chi = \frac{P}{2\sqrt{\pi A}}, \quad (4)$$

similar to Gergely et al. (2017) so that  $\chi$  of a sphere is 1.  $\chi$  was originally proposed by Garrett and Yuter (2014), who included the inter pixel variability (the variability in brightness of one pixel compared to its neighbors) in their definition, which is not  
 265 available for PIP measurements. Garrett and Yuter (2014) quantify riming based on  $\chi$ , where rimed particles (graupel) are defined as  $\chi \leq 1.35$ , moderately rimed particles as  $1.35 < \chi \leq 1.75$  and aggregates with negligible riming as  $\chi > 1.75$ .

A disadvantage of using  $\chi$  to quantify riming is that it is a purely optical measure and no physical quantity. Also, it should be taken into account that  $\chi$  not only depends on a particle's shape (closely linked to its riming degree), but also its size in pixel. Depending on the resolution of the imager as well as the exact definition of a perimeter pixel (continuous line vs. only touching  
 270 outside),  $\chi$  values of a circle with a diameter larger than 10 pixel can range from slightly below 0.9 to 1.3. Particle features finer than the resolution of the imager are not captured. This leads to smaller ratios of perimeter to area than for the same particle observed with a higher resolution imager. For better visualization, the reader may imagine a fractal shaped snowflake: the higher the resolution of the snowflake image, the larger the perimeter not only in pixel numbers, but also when converting to a physical length. For any fractal shape, the length of the shape increases, with increasing resolution resulting in an infinitely  
 275 large perimeter for an infinitely high resolution. In turn, larger particles have larger  $\chi$  than smaller particles of the exact same

shape captured by the same imager. Therefore, we take  $D_{\max}$ ,  $A$ , and  $P$  in the unit of pixel number to account for the different resolutions of CIP and PIP.

We use the same data set of simulated rimed aggregates from Maherndl et al. (2023a) to relate particle complexity  $\chi$  and size to  $M$ . Only taking simulated aggregates of dendrites, we calculate  $\chi$  from the average perimeter and area pixel counts over projections in the xy, yz and zx plane, where one pixel corresponds to a square with 20  $\mu\text{m}$  side lengths. We then derive an empirical relation with  $R^2 = 0.94$  of  $\chi$  depending on  $M$  and  $D_{\max}$  in pixel resulting in:

$$\chi = 1.33 - 0.00243 \cdot \log_{10}(M) \cdot D_{\max} + 0.000171 \cdot D_{\max} - 0.0854 \cdot \log_{10}(M), \quad (5)$$

$$\log_{10}(M) = \frac{1.33 - \chi + 0.000171 \cdot D_{\max}}{0.00243 \cdot D_{\max} + 0.0854}. \quad (6)$$

$\chi$  is calculated from CIP and PIP measured  $P$  and  $A$  for each detected particle.  $M$  is then calculated from  $D_{\max}$  and  $\chi$  for each particle. To avoid unrealistic values, we set all  $\log_{10}(M) > 0$  to 0 and all  $\log_{10}(M) < -3.5$  to -3.5. The latter threshold is chosen based on the minimum  $M$  of the combined method results.

By applying the relation derived for synthetic particles with a 20  $\mu\text{m}$  resolution to CIP and PIP measurements with 15  $\mu\text{m}$  and 103  $\mu\text{m}$  resolution, respectively, we assume the ice particle shape to be fractal - i.e.,  $\chi$  only depends on  $D_{\max}$  in pixel (and  $M$ ) and not  $D_{\max}$  in a physical length unit. To check this assumption, we decreased the "resolution" of the synthetic ice particles to 60  $\mu\text{m}$  by grouping together three by three pixels and applied Eq. 6. The resulting  $M$  bias is 27 % and in the same range as using the original 20  $\mu\text{m}$  particles (21 %).

The detection efficiency of particles that do not touch the edges of the OAPs is size-dependent: larger particles are more likely to touch the edge and therefore less likely to be detected than smaller particles. To account for this, we derive weighting factors for CIP and PIP, respectively, by comparing the count of total particles detected (including particles that touch edges) to the count of particles that do not touch edges. The weighing factors are derived for particle size bins from 10 to 65 pixel in 5 pixel bins (see Tab. C1 in Appendix C). From the calculated  $M$ , we obtain the weighted average for 1 s time steps. Then, a rolling average of 30 s (corresponding to 1.8-2.4 km for the typical Polar 6 flight speed of 60-80  $\text{ms}^{-1}$ ) is applied to make the results comparable with the  $M$  retrieval described in the previous section. We only consider particles with diameters larger 14 pixel, which correspond to 210  $\mu\text{m}$  for the CIP and 1400  $\mu\text{m}$  for the PIP. The threshold of 14 pixel was chosen such that 99 % of Polar 6 CIP and PIP measured particles with  $\chi$  smaller than 1 lie below the threshold and are therefore sorted out for the analysis.  $\chi$  values smaller than 1 are due to the low pixel resolution. This leaves us with a gap in the size range from about 1.0 to 1.4 mm. Evidently, only a subset of particles detected by CIP and PIP can be used to calculate  $M$ . Therefore, the in situ method can only be applied to a subset of the in situ data that is used for the combined method. This raises the questions of how many particles per second are enough to achieve reasonable results assuming that high enough particle counts minimize effects of the data gap. By comparison to the combined method in addition to manual inspection of CIP and PIP images, we find that in sum at least 7 particles per second need to be observed for reliably calculating  $M$  and thus we discard data with lower counts.

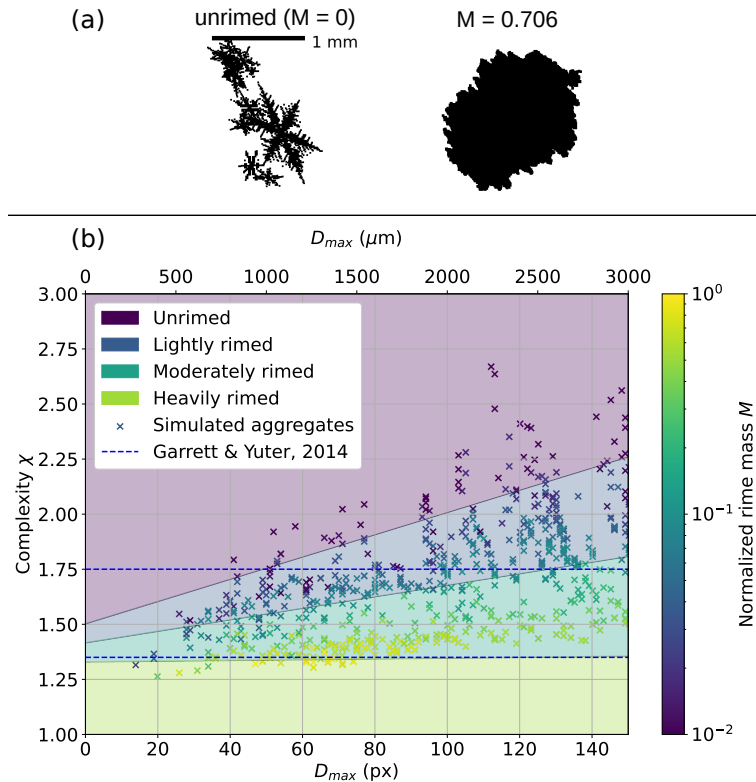


**Figure 4.** (a) Example simulated particles: unrimed dendrite aggregate (left) and moderately rimed dendrite aggregate (right). (b) Complexity  $\chi$  of simulated dendrite aggregates with different amounts of riming versus their size  $D_{max}$  in pixel. 1 pixel corresponds to the resolution of the cubic elements ( $20 \mu\text{m}$ ) that the simulated ice particles are composed of. Their normalized rime mass  $M$  is color coded.  $\chi$  thresholds for graupel (1.35) and rimed particles (1.75) from Garrett and Yuter (2014) are included as blue dashed lines. Grey lines separating differently colored areas indicate isolines of  $M$  calculated with Eq. (6):  $M = 0.01$  between unrimed and lightly rimed,  $M = 0.1$  between lightly and moderately rimed and  $M = 1.0$  between moderately and heavily rimed (graupel).

We classify particles with  $M \geq 1.0$  as heavily rimed (graupel; Fig. 4 (b)).  $M$  values larger 1.0 are physically possible and indicate rime densities larger than assumed in the aggregation and riming model ( $\rho_{\text{rime}} = 700 \text{ kgm}^{-3}$ ). Particles with  $M < 0.01$  are classified as unrimed or having negligible riming, due to their similar behavior to unrimed particles in Mahernndl et al. (2023a). In between, we call particles with  $0.01 \leq M < 0.1$  lightly rimed and with  $0.1 \leq M < 1.0$  moderately rimed (Fig. 3.2 (a), right). In most cases, unrimed particles (Fig. 4 (a), left) have much more complex shapes and therefore larger  $\chi$ , than more heavily rimed ones (Fig. 4 (a), right), which are almost spherical ( $\chi$  close to 1). Fig. 4 (b) shows the size dependency of  $\chi$ .  $\chi$  for the most heavily rimed particles, which reach  $M$  of about 0.87, is close to 1.33. Not shown are  $\chi$  values of in situ measured cloud particles, which span values from about 0.7 to 5.0 with the majority of data (95%) in the range of 1.0 to 3.0 for the CIP and 0.8 to 2.0 for the PIP.

## 4 Results and discussion

To investigate the performance of both methods, we first compare  $M$  results for collocated flight segments showing agreement in a statistical sense (Sect. 4.1). Using a case study of a collocated flight segment, we discuss under which flight conditions, agreement in a temporal sense can also be achieved (Sect. 4.2). Then, we relate  $M$  to meteorological as well as cloud micro- and macrophysical parameters to 1) further discuss possible biases of either method under certain conditions, and 2) study the occurrence of riming during collocated HALO-(AC)<sup>3</sup> segments (Sect. 4.3). We then repeat the analysis for in situ method results derived for the complete Polar 6 data set (Sect. 4.4) to show that the subset of collocated flight segments are representative for the whole campaign excluding low flight segment below 150 m.

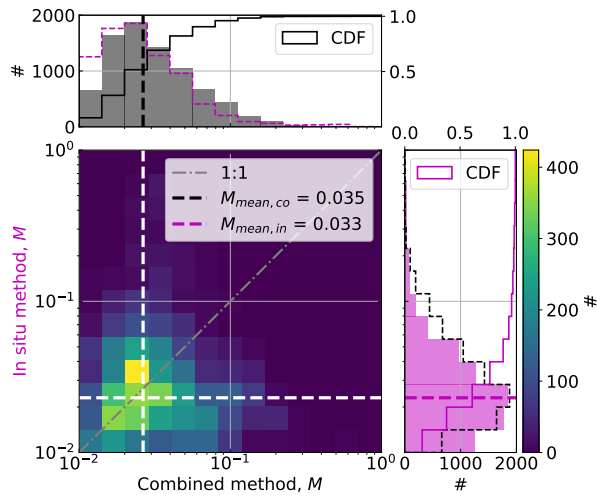
### 4.1 Statistical comparison of both methods during collocated flight segments

Figure 5 shows a 2D histogram of combined and in situ method results of  $M$  for all collocated flight segments as well as their respective  $M$  distributions. A high density of data points lies close to the 1:1 line, but data point per data point perfect agreement could not be achieved. However the latter cannot be expected: although we match remote sensing and in situ data points as best as possible, there still remain offsets in time (less than 5 min) and space (less than 5 km). Additionally, radar and in situ probes have different measurements volumes.

The respective distributions look very similar in shape, but combined method results are shifted to slightly larger values than in situ method. The mean of  $M$  is 0.035 and 0.033, the median is 0.021 and 0.024 and the 25 % to 75 % quantile ranges are 0.016 to 0.042 and 0.014 to 0.035 for combined and in situ method, respectively. The similarity in addition to the close agreement of means, medians, and quantile ranges gives us confidence that we achieve agreement with both methods and both can be used to quantify riming. Mean error (ME) and root mean square error (RMSE) are 0.0026 and 0.031 for the point by point comparison. While we do not achieve good point by point agreement (large RMSE), both methods agree in a statistical sense (small ME).

Assuming particles with  $M < 0.01$  having negligible riming, we derive average rimed fractions of 88 % and 87 % over all collocated flight segments with the combined and the in situ method, respectively. These numbers appear quite high, however, they depend heavily on the rimed vs. unrimed threshold that is chosen; if we assume  $M < 0.05$  to be unrimed instead of  $M < 0.01$ , we get 11 % and 9 % rimed particles, respectively. 12 % and 13 % of particles have  $M < 0.01$  for the combined and in situ method, respectively, 83 % and 83 % fall in range  $0.01 \leq M < 0.1$ , and only 5 % and 3 % have  $M \geq 0.1$ .

We see similar results when comparing the individual flights except for 10 April (Fig. 6). Manual inspection of CIP and PIP images shows a high proportion of rimed particles during the collocated segment on 10 April (not shown), which is in agreement to the combined method. These particles appear to predominately have sizes around 1 mm – large enough to often touch edges in CIP images, but too small to be able to calculate  $\chi$  from PIP images. In all further analysis steps, we exclude the April 10 data, which corresponds to 6 minutes of collocated data.



**Figure 5.** 2D histogram of  $M$  derived with combined (x-axis, black) and in situ (y-axis, magenta) methods in logarithmic units during collocated flight segments. Individual histograms and cumulative distribution functions (CDF) are included in black for the combined (top panel) and in magenta for the in situ method (right panel). Combined and in situ method histograms are also included as dashed lines in their respective color. Respective medians are plotted as dashed lines.

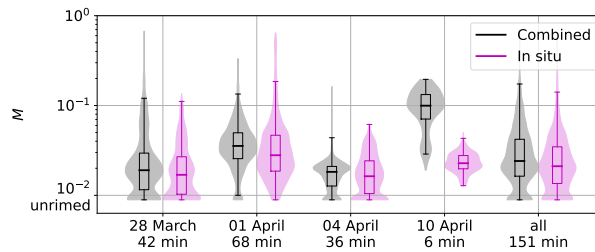


**Figure 6.** Box plots superimposed violin plots showing distributions of  $M$  in logarithmic units derived with combined (black) and in situ method (magenta) for collocated flight segments on the respective flight day and in total for all regarded collocations. Approximate collocated flight time in minutes is included.

## 4.2 Case study: collocated segment, 01 April

The good statistical agreement between both methods in combination with a rather large RMSE raises the question of why  
350 agreement in terms of temporal co-fluctuations could not be achieved for all flight segments. In the following, we use a case  
study to demonstrate under which conditions combined and in situ method agree on a data point per data point basis and discuss  
possible biases of both methods.

A high pressure system north of Greenland and a strong low pressure complex north of Siberia lead to northerly and north-  
easterly winds almost parallel to the ice edge in the Fram Strait, where the measurements were performed. The movement  
355 of cold air from the colder sea ice north of the Fram Strait to the warmer ocean resulted in the formation of cloud streets,  
which can be seen in Fig. 7 (a). Walbröl et al. (2023) could identify this cold air advection as a strong marine cold air outbreak  
(MCAO) that lasted from 01 to 02 April. On 01 April, Polar 5 and Polar 6 conducted collocated flights, crossing the Fram Strait  
perpendicular to the cloud streets from 7.6 °E to 1.5 °E back and forth three times. Clouds were thicker, more pronounced and  
extended higher over the open ocean on the eastern side of these segments than close to the MIZ and were absent over sea  
360 ice. Polar 5 stayed at a constant altitude of 3 km, while Polar 6 performed predominately staircase patterns measuring in and  
above clouds. Here, we show a short segment where Polar 6 flew inside clouds from west to east on the eastern side of the  
measurement area close to 7.6 °E, while Polar 5 flew above. Then, both aircraft turned and flew the same way back westward.  
Excluding the turn, the horizontal distance between both airplanes ranged from 48 m to 2.7 km and was on average 1.2 km.

A detailed view of collocated in situ and radar measurements during this segment is presented in Fig. 8. The first column  
365 shows measurements before the turn (aircraft flying from west to east, about 11:08 to 11:18 UTC), while the second column  
shows measurements after the turn (east to west, about 11:25 to 11:35 UTC). We cut out the turn due to unreliable measurements  
and/or collocation matching when the radar is tilted due to the aircraft roll. In-cloud temperatures decreased with height ranging  
from  $-22^{\circ}\text{C}$  to  $-15^{\circ}\text{C}$  in the measured area (Fig. 8 (e) and (f)). The cloud's roll structure is clearly visible in the radar  
measurements:  $Z_e$  shows periodic streaks of high and low values (Fig. 8 (c) and (d)), which can also be seen in the averaged  
370 (moving over 30 s), corrected  $Z_e$  at the altitude of Polar 6 (Fig. 8 (a) and (b)).  $D_{32}$  is the proxy for the mean mass-weighted  
diameter (e.g. Maahn et al., 2015) and is defined as the ratio of the third to the second measured PSD moments  $M_3/M_2$   
assuming a typical value of 2 for the exponent  $b$  of the mass-size relation (e.g., Mitchell, 1996).  $D_{32}$  calculated from the 30 s  
running average of the combined in situ PSD (Fig. 8 (g) and (h)) and the PSD (Fig. 8 (i) and (j)) show gaps when Polar 6 was  
flying close to cloud top (before the turn) and streaks of high  $Z_e$  appear to correlate with increases in  $D_{32}$ . Nevzorov probe  
375 measurements (Fig. 8 (k) and (l)) show that the sampled cloud was mixed-phase with LWC being in general slightly higher  
close to cloud top.

We see good agreement when looking at mean, median, and quantile ranges of  $M$  derived with combined and in situ method  
before and after the turn. The combined method results in median (mean)  $M$  of 0.031 (0.040) before and 0.032 (0.037) after  
the turn, while the in situ method gives median (mean)  $M$  of 0.031 (0.033) before and 0.022 (0.031) after the turn. 25 % to  
380 75 % quantile ranges are 0.022 to 0.044 and 0.024 to 0.042 for the combined method before and after the turn, respectively.  
Quantiles range from 0.021 to 0.043 and 0.018 to 0.036 for the in situ method.

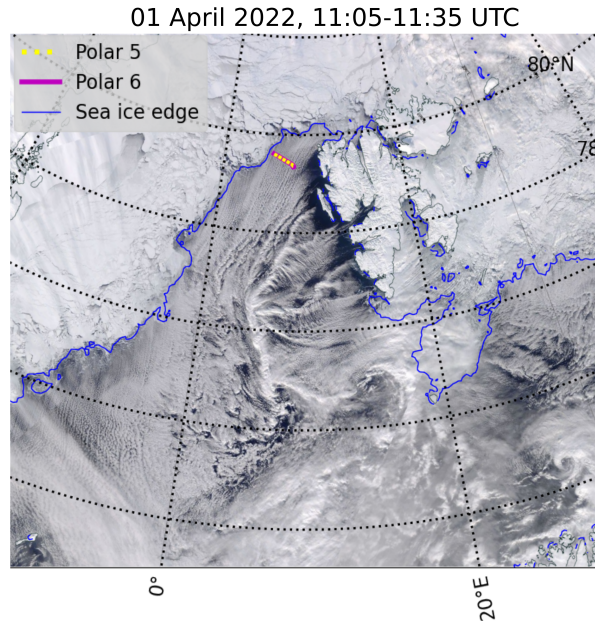


**Figure 7.** MODIS Terra reflectance images (NASA worldview) from 01 April. The flight tracks of Polar 5 (yellow) and Polar 6 (magenta) as well as the sea ice edge (15 % SIC) of the same day are included.

However, when comparing the time series of  $M$ , we see a much better agreement in terms of temporal confluations after than before the turn. We assume that the discrepancy before the turn is due to the Polar 6 measurements being close to the upper edge of the cloud. As discussed in Appendix D, agreement between both methods is worse close to the highest radar range gates with cloud signals. This is likely due to the higher spatial variability and larger spatial gradients of cloud properties. Even slight horizontal offsets of Polar 5 and Polar 6 in addition to the different measurement volumes of radar and cloud probes can result in disagreements between radar and in situ probes. Close to the upper edge of the cloud this can result in the radar detecting a gap in cloud while the in situ probes measure a particle concentration larger than zero or vice versa. Apparently, the running averages of 30 s on both data sets cannot completely resolve this problem. In addition, median particle count increases from 17 before the turn to 22 after the turn, resulting in the in situ method being less reliable before the turn as well. Therefore, near cloud top, both methods are less reliable in a spatio-temporal sense. They do, however, both produce reliable estimations of  $M$  in a statistical sense.

After the turn, combined and in situ results for  $M$  show better agreement as Polar 6 was flying deeper in the cloud under more homogeneous conditions. Both methods show an almost periodic in- and decrease of  $M$  with (almost) matching maxima and minima in extent and location. Compared to  $Z_e$  (Fig. 8 (b) and (d)), high  $M$  correlate with high  $Z_e$  indicating that riming plays a dominant role in MPC variability as observed by radar.

CIP and PIP images taken at 7.0 °E after turn are presented in Fig. 8 (o) and (p) and show a mixture of small liquid drops, pristine plates and a high proportion of rimed (aggregated) dendritic ice particles explaining the peak in  $M$  for both methods.



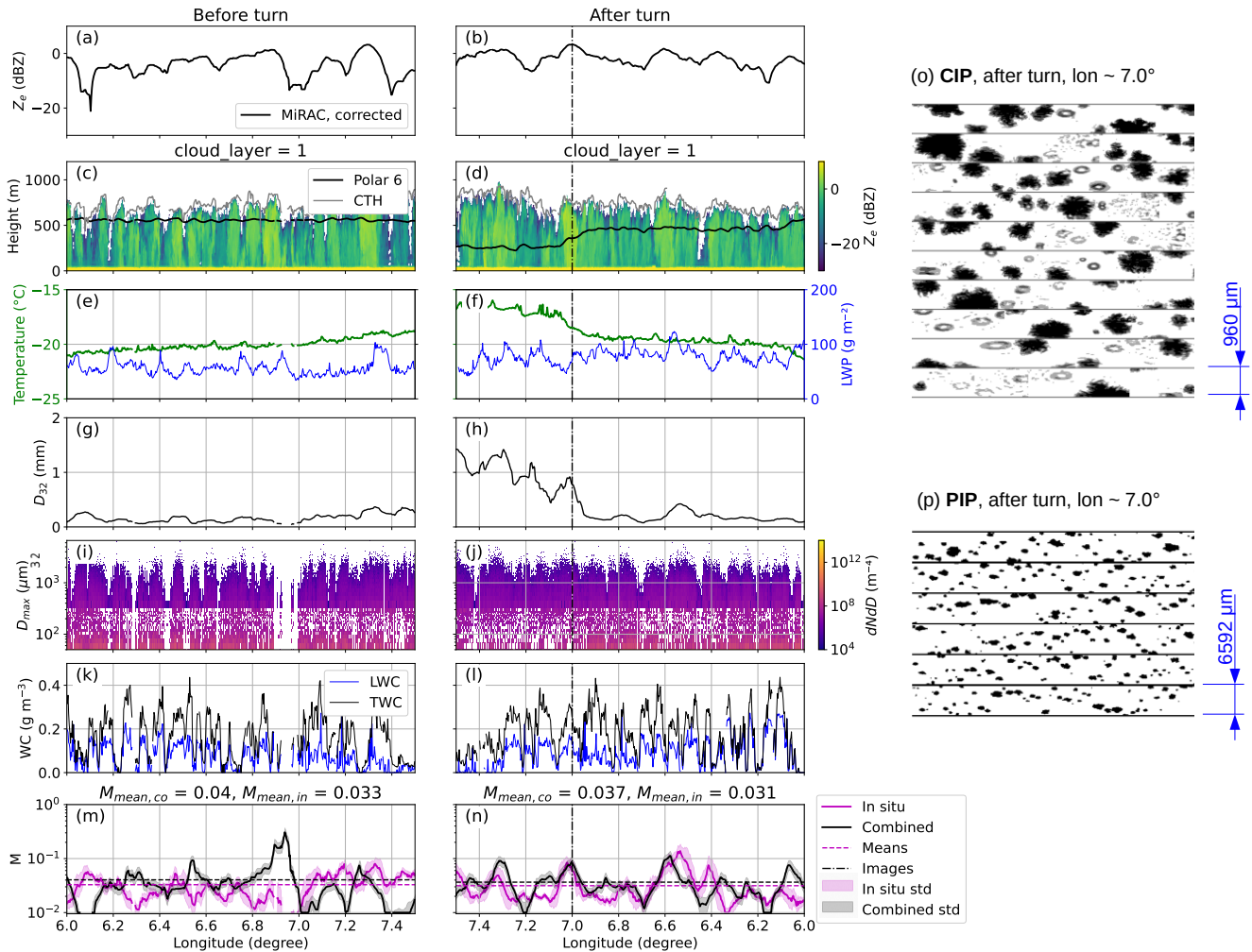


**Figure 8.** Collocated flight segments from 01 April 11:05-11:35 UTC before (first column) and after turn (second column). The longitude axis is reversed for the after turn segment to visualize time passing on the x-axis. (a)-(b) MiRAC measured and corrected reflectivity  $Z_e$  in flight altitude of Polar 6; (c)-(d) MiRAC measured reflectivity  $Z_e$ , AMALi CTH, and Polar 6 flight altitude; (e)-(f) Polar 6 noseboom temperature (green) and MiRAC-A LWP (blue); (g)-(h) mass-weighted diameter  $D_{32}$  derived from the 30 s running averaged combined in situ PSD; (i)-(j) CIP and PIP measured combined PSD (not-averaged); (k)-(l) Nevzorov probe LWC (blue) and TWC (black); (m)-(n)  $M$  from combined (black) and in situ method (magenta) including uncertainty estimates (combined: OE standard deviation, in situ: 30 s running standard deviation); (o) example CIP; (p) PIP images from  $7^\circ\text{E}$  after the turn as indicated by the dash-dotted line in panels (b), (d), (f), (h), (j), (l), and (n).

### 4.3 Occurrence of riming during collocated flight segments

400 Figure 9 gives an overview of the occurrence of riming depending on (a)-(d) Polar 6 nose boom measurements of air temperature  $T$ , (e)-(h) Nevzorov probe LWC, (i)-(l) Nevzorov probe TWC, (m)-(p) MiRAC-A retrieved LWP, and (q)-(t) the normalized position of Polar 6 in cloud, which we define as the fraction of Polar 6 flight altitude minus cloud bottom height (CBH) and CTH minus CBH (therefore: cloud bottom = 0, cloud top = 1). CTH is determined from AMALi, while CBH is determined from radar measurements, where cloud bottom is the lowest  $Z_e$  measurement not affected by ground clutter. If there  
405 is a continuous signal from 150 m to the flight altitude of Polar 6, then cloud bottom is set to 150 m. Note that the liquid cloud base which is commonly used when using ground-based remote sensing, is not available for airborne measurements. Our cloud definition includes precipitation falling out of the cloud liquid layer so that a multi-layer clouds connected by precipitation would be treated as a single cloud. During the collocated flight segments used in this study, no separate cloud layers were observed by the radar above Polar 6. The average rimed fractions derived with both methods show a similar behavior for all  
410 parameters and lie on average within 6 percentage points of each other. Linear medians match within a factor of 0.3 of each other.

When analyzing the relation of riming with temperature, moderate riming also occurs at low temperature below  $-15^\circ\text{C}$ . Between  $-10$  and  $-15^\circ\text{C}$ , (local) minima of rimed fractions and  $M$  are evident with both methods. This coincides with the so-called dendritic growth zone, where aggregation is favored (Takahashi et al., 1991; Takahashi, 2014). Complex aggregated  
415 forms can appear round when viewed from certain angles and imaged with a limited resolution. This might lead to an overestimation of riming with the in situ method. Note that only the temperature at the point of observation is available, not where – at potentially colder temperatures – the riming process itself took place. The disagreement above  $-10^\circ\text{C}$  stems from a 10 minute flight segment on 04 April where in situ method  $M$  results go slightly below 0.01, while combined method  $M$  stay slightly above 0.01. Median (25-75 % quantile range)  $M$  are 0.019 (0.016-0.020) and 0.012 (0.006-0.016) for combined and in situ  
420 method, respectively.

There is no clear dependence of riming on LWC. The rimed particles could easily have undergone riming in a SLW layer above and fallen out to a place in the cloud with little to no SLW. Rimed fraction only increase slightly with TWC. This is likely because  $M$  results are low for the whole campaign and large, unrimed aggregates can also result in large TWC.

For LWP, median  $M$  and rimed fractions increase with increasing LWP up until  $50\text{ gm}^{-2}$  and decrease in the two highest  
425 LWP bins. This decrease could be due to limited sampling as the bins contain less than 500 data points. Overall, the agreement between both methods is very good with rimed fraction agreeing on average within 3 percentage points below and 11 percentage points above  $100\text{ gm}^{-2}$ .

Riming fractions agree within 2.7 percentage points for in cloud position above 0.2 (meaning Polar 6 is flying higher than the lowest 20 % of the cloud). Below 0.2, rimed fractions derived by the in situ method are on average 19.5 percentage points  
430 lower than by the combined method. However, median  $M$  agree within a factor 0.29 above and 0.17 below 0.2. Because our definition of a cloud includes precipitation below, low cloud positions might be below the liquid cloud base. If this is indeed the case, we expect the falling particles to be larger and heavier than the particles in the cloud above. The detection efficiency

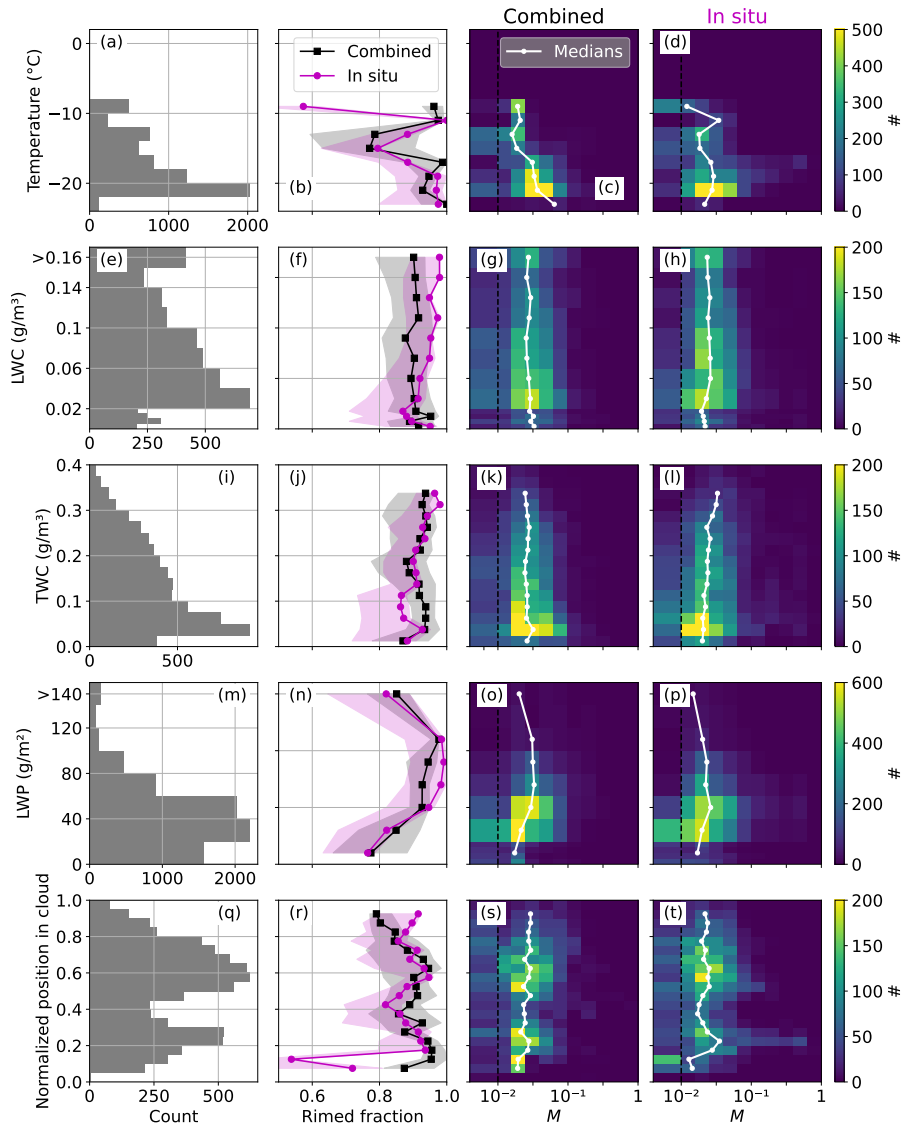


**Figure 9.** Occurrence of riming during collocated flight segments derived with combined (black) and in situ method (magenta) depending on (a)-(d) Polar 6 noseboom temperature in  $^{\circ}\text{C}$ , (e)-(h) Nevzorov probe measured LWC in  $\text{g}/\text{m}^3$ , (i)-(l) Nevzorov probe measured TWC in  $\text{g}/\text{m}^3$ , (m)-(p) MiRAC-A retrieved LWP in  $\text{g}/\text{m}^2$ , and (q)-(t) normalized position of Polar 6 in cloud (0 meaning bottom of cloud, 1 meaning top of cloud). Bin sizes are 2 K,  $0.02 \text{ g}/\text{m}^3$  ( $0.005 \text{ g}/\text{m}^3$  below  $0.02 \text{ g}/\text{m}^3$ ),  $0.025 \text{ g}/\text{m}^3$ ,  $20 \text{ g}/\text{m}^2$ , and 0.05 respectively. The first column shows the amount of data per bin. The second column shows rimed fraction assuming  $M < 0.01$  to be unrimed derived with combined (black squares) and in situ method (magenta circles). Uncertainty estimates are shaded (combined: OE standard deviation, in situ: 30 s running standard deviation). The third and fourth columns show 2D histograms of  $M$  results for combined and in situ method, respectively, including medians for each bin in white. The black dashed line shows  $M = 0.01$ . All values with  $M < 0.01$  are grouped together in the lowest bin. Medians and average rimed fractions are only shown, when there are more than 100 data points per bin. Nevzorov probe data is only available in April.

of cloud probes is worse for particles close to the upper end of their size range, even if we count particles that touch edges (as is done in the PSD calculation). Therefore the higher rimed fractions obtained by the combined method could be due to missing large particles in the PSD that the radar can see. The Optimal Estimation retrieval would then overcompensate by increasing  $M$ , resulting in a higher amount of rimed particle populations for the combined method. Averaging the in situ data for longer time spans should ensure capturing more large particles. Using running averages of 60 instead of 30 s shifts the rimed fractions below 0.2 only slightly closer together (agreement within 18.8 percent points; not shown). However, average particles sizes increase at small normalized positions in cloud. Median values of  $D_{32}$  increase by about 150 % from 1.52 mm at 0.15-0.2 to 3.71 mm at 0.05-0.1. Disagreement between both methods is higher, when Polar 6 is flying near the top of the radar signal (Fig. D1) due to the higher variability of measurements as we show in Appendix (D).

#### 4.4 In situ only flights

Here, we extend the analysis to periods only covered by the in situ aircraft to analyze how representative of the complete Polar 6 data the collocated measurements are. Even though a large, unique data set of collocated, airborne measurements was collected in the Arctic during HALO-(AC)<sup>3</sup>, the total number of in situ cloud measurement time exceeds the collocated measurement time by a factor of 5. Figure 10 shows the dependence of  $M$  on temperature and LWC as in Fig. 9 but for the extended in situ data set. The position of Polar 6 in-cloud as well as MiRAC-A retrieved LWP must be omitted due to the missing Polar 5 remote sensing information. TWC is not shown due to not adding further information as discussed in Sect. 4.3. The average rimed fraction assuming  $M < 0.01$  ( $M < 0.05$ ) to be unrimed is 69 (13) % with a mean  $M = 0.030$ , median  $M = 0.016$  and a 25 % to 75 % quantile range of 0.009 to 0.031. These values are slightly lower and indicate a slight shift towards more riming during the collocated segments.

When focusing on temperature bins with a sufficiently high number of observations, we observed decreasing riming from -10 and -16 °C with decreasing temperature (Fig. 10 (b)). The rimed fraction for all in situ flights follows a similar shape to the collocated sub-sample in that temperature range, albeit with a lower local maximum at -11 °C (0.72 vs. 1.0). There is a slight local minimum of median  $M$  and rimed fraction at about -14 °C. Lower rimed fractions and median  $M$  result for lower temperatures when including all Polar 6 data. Similarly, rimed fraction and median  $M$  are lower for LWC below 0.05 gm<sup>-3</sup>.

Differences between the in situ method results for only collocated vs. all segments are smaller when excluding Polar 6 data below 150 m as can be seen in Fig. 10: the rimed fraction curve is shifted towards larger values. Also, both rimed fraction vs. LWC curves are very close, deviating by a maximum 5.4 percentage points. The better agreement above 150 m could be simply due to the higher proportion of common data points because the collocated in situ method  $M$  is a subset of the in situ method  $M$  derived for all Polar 6 flight segments. Another explanation could be the influence of cloudless ice crystal precipitation ("diamond dust"). This phenomenon describes the formation of ice crystals under clear or nearly clear skies. Diamond dust typically occurs between November and mid-May in heights below 250 m over the Arctic Ocean (Intrieri and Shupe, 2004). This could shift the curve towards less riming for cold temperatures, resulting in an (almost) disappearance of the -15 °C local minimum.

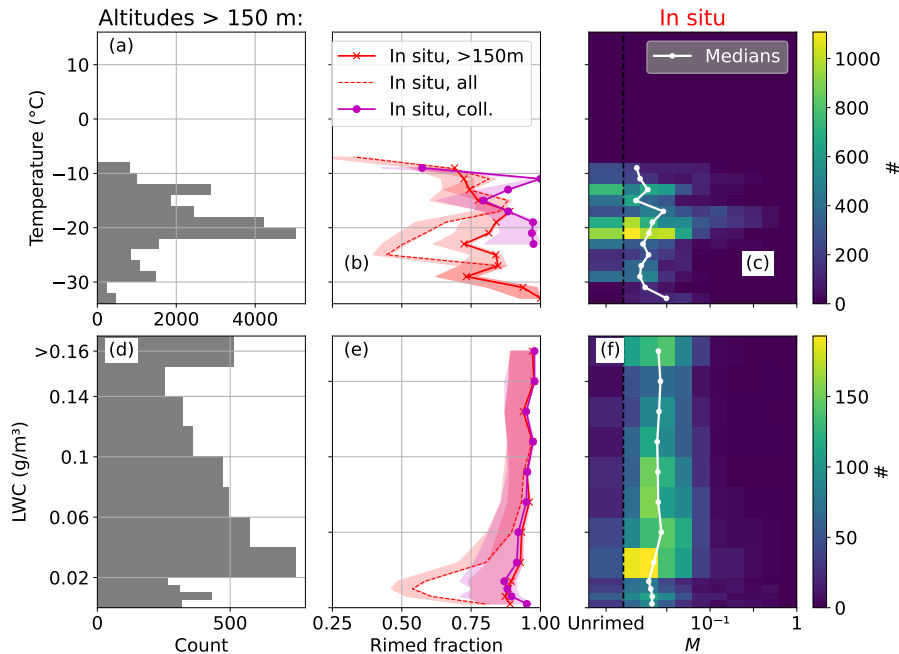


**Figure 10.** As Fig. 9 (a)-(h), but only the in situ method for all Polar 6 flights with altitudes above 150 m. Rimed fractions for all flight segments are shown as red crosses, whereas results for collocated flights are repeated as magenta circles in (b) and (e). All data including flight altitudes below 150 m are shown as red dashed lines. Nevzorov probe data is only available in April.

We can conclude that the collocated flight segments are in part representative of all Polar 6 flight segments where Polar 6 flew above 150 m: they show similar behavior in terms of  $M$  dependence on LWC. However the collocated segments are biased towards higher amounts of rimed particles at low temperatures below  $-17^{\circ}\text{C}$ .

## 5 Conclusions

470 In this study, we present two methods to quantify riming with the normalized rime mass  $M$  using airborne in situ and re-  
 mote sensing observations. We apply both methods to data collected during the HALO-(AC)<sup>3</sup> field campaign performed in  
 March/April 2022. One objective of HALO-(AC)<sup>3</sup> was performing collocated flights with up to three aircraft. We focus on the  
 research aircraft Polar 5 and Polar 6, which collected closely spatially collocated and almost simultaneous in situ and remote  
 sensing observations west of Svalbard.

475 The first method takes advantage of these collocated flight segments to derive  $M$ . We developed an Optimal Estimation  
 algorithm to retrieve  $M$  from a combination of radar and in situ measurements by matching measured with simulated radar  
 reflectivities  $Z_e$  obtained from observed in situ particle number concentrations. As forward operator we use the Passive and  
 Active Microwave radiative TRAnSfer tool (PAMTRA) which includes empirical relationships of  $M$  and particle properties

from Maherndl et al. (2023a) for estimating particle scattering properties. The latter are obtained via aggregation and riming  
480 model calculations.

With the second method,  $M$  can be derived from in situ measured particle shape alone. We calculated the complexity  $\chi$  of in  
situ measured particles, which relates particle perimeter to area. Further, we derived  $M$  from empirical relationships that were  
again obtained from synthetic particles. However, we find that this method is only reliable when sufficient numbers of particles  
large enough to calculate meaningful  $\chi$  are detected with the in situ probes. A threshold of 7 particles per second appears to  
485 result in a good performance.

We compare the obtained  $M$  derived by both methods: combined and in situ methods result in median (mean)  $M$  of 0.024  
(0.035) and 0.021 (0.033) during collocated segments,  $M$  distributions look remarkably similar. However, data point per data  
point agreement could not be achieved for all flight segments. Looking at each flight with collocation individually, we find  
similar results except for 10 April when the combined method shows higher  $M$  than the in situ method. By visual inspection  
490 of CIP and PIP images for the 6 minutes of collocated measurements, we find the higher  $M$  predicted by the combined method  
to be closer to the truth. Likely, the in situ method performs worse, because a significant amount of rimed particles fall into the  
size range that cannot be used, i.e. particles are too large for the CIP but too small to derive  $\chi$  from PIP.

Using a case study, we show that we achieve good agreement in terms of temporal confluctuations as long as measurements  
are homogeneous, which is more often the case when Polar 6 is flying deeper in the cloud. Under inhomogeneous conditions,  
495 both methods agree in a statistical sense.  $M$  appears to increase and decrease periodically in correspondence with  $Z_e$ , indicating  
that riming plays an important role in the  $Z_e$  variability, which is commonly observed in Arctic MPC.

In addition, we analyzed the dependence of  $M$  on air temperature, LWC, LWP, and the position of Polar 6 in the cloud.  
Rimed fractions (assuming  $M < 0.01$  to be unrimed) agree on average within 7 percentage points. With either method, we  
do not find a clear relation of LWC and riming during the collocated segments. LWP shows a positive correlation with riming  
500 below  $130 \text{ gm}^{-2}$ . We confirm findings from Fitch and Garrett (2022), which show that riming also occurs in Arctic clouds with  
low LWP. Both methods show a decrease in riming at about  $-15^\circ\text{C}$ , which corresponds to the dendritic growth zone (Takahashi  
et al., 1991; Takahashi, 2014). When extending the in situ method to all Polar 6 flights, these findings hold as long as low flight  
segments are excluded. Close to the upper edge of the radar signal (cloud top as seen by the radar reflectivity measurements),  
the methods disagree, especially when comparing data point per data point. The combined method shows higher rimed fraction  
505 and  $M$  than the in situ method (Fig. D1). We think that this is likely due to the higher variability of cloud properties at cloud  
top resulting in less tolerance of the results to the collocation of Polar 5 and Polar 6. Disagreement is also larger close to cloud  
bottom, which includes precipitation below the cloud, due to detection of the liquid cloud base being unavailable from the  
aircraft measurements. We think that large particles that are missed by the cloud probes due to detection efficiency but seen by  
the radar might be the reason for higher riming fractions from the combined method. Median values of  $D_{32}$  over all collocated  
510 segments increase by about 150 % from 1.52 mm at a normalized position in cloud of 0.15-0.2 to 3.71 mm at 0.05-0.1.

With both methods, we derive average  $M$  over the particle population observed at a given time step. However, we often  
observed mixtures of pristine and rimed particles of different sizes during the campaign. While we correct the in situ method  
 $M$  accounting for the size dependent detection efficiency of CIP and PIP, we are still left with a size gap between probes.  $M$

515 results obtained with the in situ method are therefore biased towards smaller particles than 1 mm as well as larger particles  
than 1.4 mm. Because  $Z_e$  is more sensitive to large particles,  $M$  derived by the combined method is likely skewed towards the  
right tail of the PSD. In future studies, the in situ method can be adapted to derive size distributions of  $M$  (given the particle  
count per bin is sufficiently large) to compensate this. Additionally, implementing a particle type identification algorithm will  
likely improve uncertainties of both methods and should be investigated in future studies.

520 The presented methods provide tools to better quantify riming in MPC from airborne observations. This allows to study  
external drivers and the variability of riming.

*Data availability.* Processed in situ and radar data as well as MiRAC-A LWP and AMALi CTH from the HALO-(AC)<sup>3</sup> campaign are currently  
being prepared for publication in PANGAEA. The data can (already) be easily accessed by the python package ac3airborne (Mech et al.,  
2022b). Raw in situ cloud data recorded by the CDP, CIP and PIP are archived at the German Aerospace Center and are available on request.  
The data set of simulated rimed aggregates generated for Mahernndl et al. (2023a) is available at <https://doi.org/10.5281/zenodo.7757034>  
525 (Mahernndl et al., 2023b).

## Appendix A: Assumption on particle shape

For both combined and in situ method, we assume the particle shape to be "dendrites". Here we show results assuming "plates"  
or "columns" and discuss implications for our results. We chose to show  $M$  plots in linear scale due to the larger uncertainties  
at high  $M$  values.

530 Figure A1 shows  $M$  results for the combined method using the mass size parameter for plates and columns from Mahernndl  
et al. (2023a). We do not show rosettes or needles, because the temperature range observed during HALO-(AC)<sup>3</sup> does not favor  
these ice particle shapes (needles commonly occurring at -5 °C and warmer; rosettes at -40 °C and colder). While  $M$  results for  
columns are lower than for dendrites (Fig. A1 (a)), plates and dendrites result in the same  $M$  within the uncertainty estimates  
(Fig. A1 (b)). Although we expect the majority of data to be collected in a plate-like growth regime (92 % of collocated and  
535 81 % of total in situ cloud data was collected in a temperature range of -10 °C to -30 °C (excluding April 10)), the lower  $M$   
results for columns could explain the discrepancy between both methods at temperatures warmer -10 °C (Fig. 9 (b)).

Similarly, Fig. A2 shows in situ method  $M$  results using plates and columns to derive fit coefficients. Within uncertainty  
estimates, which are derived from the standard deviations over the 30 s averaging window,  $M$  results for columns and plates  
agree with those for dendrites. Still, we want to note that there is a positive bias for  $M$  derived for dendrites compared to plates  
540 and a negative bias compared to columns. This could further explain the discrepancy between combined and in situ method at  
temperatures above -10 °C.

As described in Sect. 3.2 we use simulated rimed aggregates from Mahernndl et al. (2023a) to derive empirical relations. For  
columns and plates the following function result (with  $R^2 = 0.92$  and  $0.93$ , respectively;  $D_{\max}$  is again in pixel):

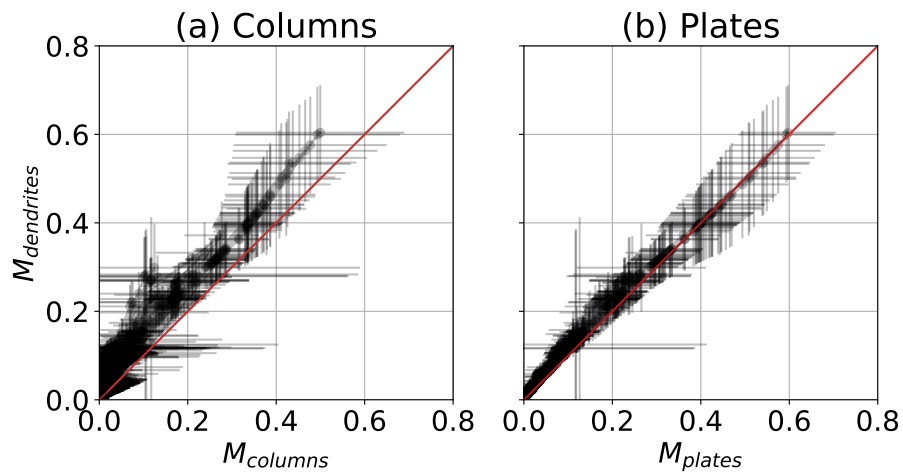


**Figure A1.** OE retrieval (combined method) results assuming mass size parameters for (a) columns  $M_{columns}$  and (b) plates  $M_{plates}$ . The 1:1 line is shown in red.

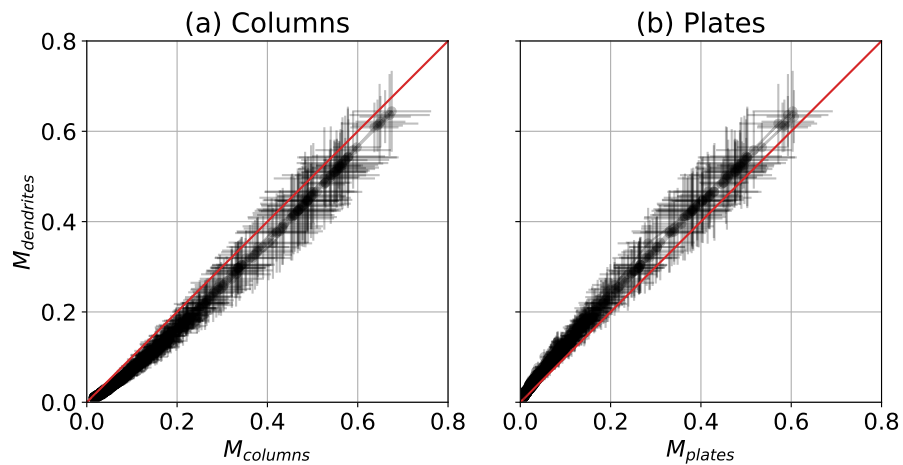


**Figure A2.** In situ method results assuming (a) columns  $M_{columns}$  and (b) plates  $M_{plates}$ . The 1:1 line is shown in red.



$$\log_{10}(M_{columns}) = \frac{1.33 - \chi + 0.0000903 \cdot D_{max}}{0.00291 \cdot D_{max} + 0.115}, \quad (\text{A1})$$

$$545 \quad \log_{10}(M_{plates}) = \frac{1.33 - \chi + 0.000223 \cdot D_{max}}{0.00291 \cdot D_{max} + 0.0370}. \quad (\text{A2})$$

## Appendix B: Validation of the combined method with synthetic data

To approximate errors of the combined method  $M$  retrieval, we present results obtained for synthetic data. We use the simulated rimed dendrite aggregates from Maherndl et al. (2023a) binned into 10 logarithmic  $M$  bins from  $10^{-2}$  to  $10^0$  ("true"  $M$ ) and linear  $D_{max}$  bins from 0 to 10 mm with bin widths of 200  $\mu\text{m}$ . We apply exponential PSDs  $N(D) = N_0 \exp(-\Lambda D)$  to each  
550  $M$  bin, where  $N$  is the number concentration in  $\text{m}^{-4}$  of particles of size  $D$  in m, the intercept parameter  $N_0$  (in  $\text{m}^{-4}$ ) describes the overall scaling and the slope parameter  $\Lambda$  controls the shape. Similar to Maherndl et al. (2023a), we derive  $N_0$  with the empirical function from Field et al. (2006) for temperatures  $T$  from -25 to -1  $^\circ\text{C}$  in 1 K steps. We calculate  $\Lambda$  from the total number of particles  $N_{tot}$  with  $\Lambda = N_0/N_{tot} \text{ m}^{-1}$  and vary  $N_{tot}$  from 500 to 4500  $\text{m}^{-3}$  in 500  $\text{m}^{-3}$  steps. This results in a total of 2250 PSDs. We use PAMTRA to calculate  $Z_e$  from the PSDs with the same set up as for the observations (see Sect.  
555 3.1). We use the exact particle masses from the aggregation and riming model results and the SSRGA parameter calculated with snowScatt (Ori et al., 2021) that were used as a reference in Maherndl et al. (2023a). The resulting  $Z_e$  are assumed to be the "truth" and referred to as  $Z_{e,true}$ .

We then apply the retrieval framework of the combined method using the generated PSD in the forward operator  $\mathbf{F}$  and  $Z_{e,true}$  as  $\mathbf{y}$ . To be consistent, we assume  $\mathbf{x}_a = -1$  (corresponding to  $M = 0.1$ ) as a-priori information,  $\mathbf{S}_a=1$  as a-priori  
560 uncertainty and  $\mathbf{S}_y$  corresponding to a measurement uncertainty of 1.5 dB. Mass-size and scattering are parameterized with the riming-dependent parameterization (Maherndl et al., 2023a). We therefore treat the synthetic data analogous to the in situ observations and pretend that the mass of the particles is unknown.

Figure B1 shows (a) the resulting  $Z_e$  derived with the OE framework plotted against  $Z_{e,true}$  and (b) the retrieved  $M$  plotted against the true  $M$ . OE  $Z_e$  has a mean bias of -0.05 dB and an absolute mean bias of 0.09 dB compared to  $Z_{e,true}$ ;  
565 both well within the assumed "measurement" uncertainties.  $M$  is overestimated slightly for low  $M_{true}$ . This stems from the slight positive bias of less than 1 dB of the riming-dependent parameterization for lightly rimed particles when applying an exponential sizes (see Fig. 10 (b) of Maherndl et al. (2023a)). In logarithmic space, the  $M$  results have a mean bias of 7.7 %, which corresponds to 20 % in linear space. The uncertainty output from the OE estimation scheme results in a state space variance  $\mathbf{S}_x$  corresponding to an  $M$  uncertainty of 7.8 % (in the logarithmic framework).

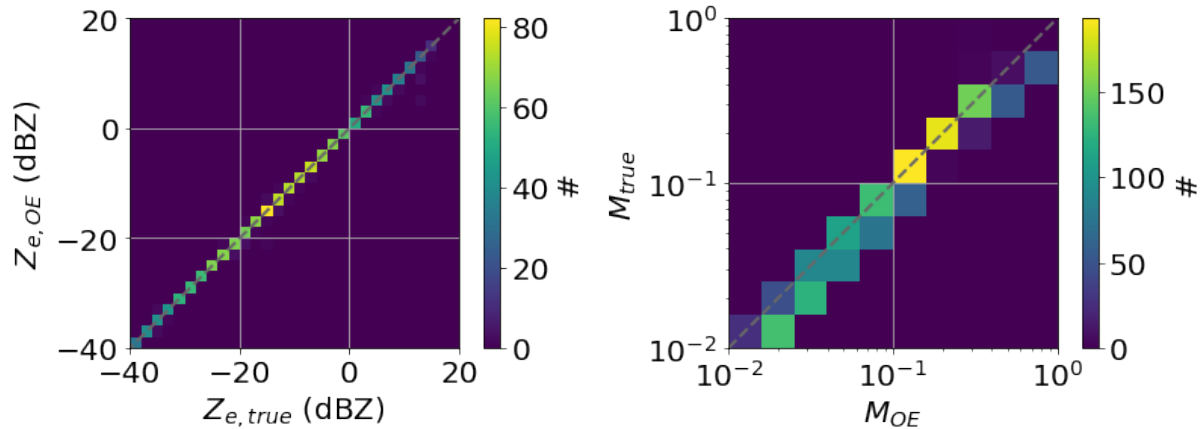


**Figure B1.** OE retrieval (combined method) results with synthetic data: (a) reflectivity  $Z_{e,OE}$  vs. reflectivity  $Z_{e,true}$  calculated with exact particle masses and snowScatt derived SSRGA parameter; (b) retrieved  $M_{OE}$  vs. true  $M_{true}$ .

**Table C1.** Weighting factors  $w_{CIP}$  and  $w_{PIP}$  that were derived to account for the size-dependent detection efficiency of the probes.

Size bin (pixel)	$w_{CIP}$	$w_{PIP}$
[10, 15)	1.53	1.24
[15, 20)	1.52	1.33
[20, 25)	1.71	1.42
[25, 30)	1.96	1.46
[30, 35)	2.35	1.53
[35, 40)	2.31	1.69
[40, 45)	2.72	1.62
[45, 50)	3.12	1.91
[50, 55)	3.64	2.19
[55, 60)	4.54	2.84
[60, 65)	6.43	5.35

## 570 Appendix C: In situ method weighting factors

Tab. C1 shows the weighing factors that were derived for CIP and PIP by comparing counts of all particles to particles that do not touch the edges of the OAPs.

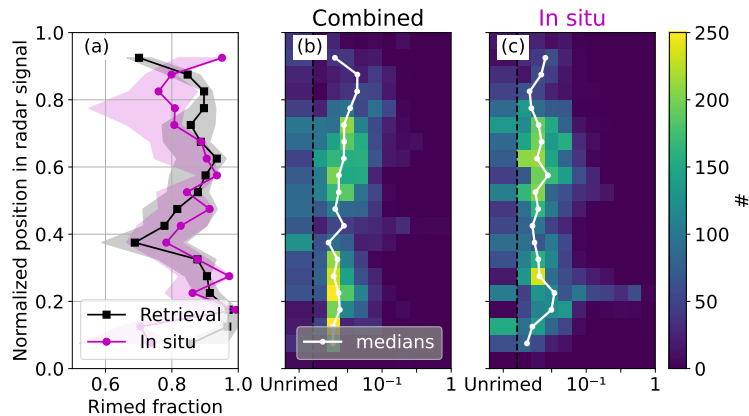


**Figure D1.** As Fig. 9 (r)–(t), but for the position of Polar 6 in the radar signal with 0 meaning cloud bottom as seen by radar (minimum 150 m due to surface clutter) and 1 meaning cloud top as seen by radar.

#### Appendix D: Limitations close to radar signal cloud top

Near the top edge of the measured radar signal, disagreement between in situ and combined method is higher (Fig. D1), which could be due to higher variability of cloud properties there: while the radar on board Polar 5 might see a gap in clouds, Polar 6 might fly a few hundred meters away in a cloudy region. Alternatively, the radar could see signatures of clouds due to its larger footprint while the cloud probes on Polar 6 measured no particles in close proximity. Both cases do not (or rarely) occur when Polar 6 is further in the cloud where cloud properties are more homogeneous. The in situ method could also be less reliable at cloud top due to lower sample sizes. Given the available data, a concluding explanation cannot be given.

**580** *Author contributions.* N. Maherndl developed the described methods to quantify riming, analyzed and plotted the data and wrote the manuscript. M. Maahn acquired funding and supervised the research project. M. Moser collected and processed CDP, CIP and PIP data and provided combined size distributions. J. Lucke collected and processed Nevzorov probe data. M. Mech and N. Risse collected and processed MiRAC-A data and retrieved the LWP product. M. Mech, N. Risse and I. Schirmacher collected and processed AMALi data and retrieved the CTH product. All authors reviewed and edited the draft.

**585** *Competing interests.* M. Maahn is a member of the editorial board of Atmospheric Measurement Techniques. The peer-review process was guided by an independent editor and the authors also have no other competing interests to declare.

*Acknowledgements.* We gratefully acknowledge the funding by the Deutsche Forschungsgemeinschaft (DFG, German Research Foundation) for the “Arctic Amplification: Climate Relevant Atmospheric and Surface Processes, and Feedback Mechanisms” (AC)3 Project

268020496–TRR 172 within the Transregional Collaborative Research Center. Contributions by M. Moser were funded by German Research  
590 Foundation (DFG, Deutsche Forschungsgemeinschaft) under the Priority Program SPP PROM Vo1504/5-1 and by TRR 301 - Project-ID  
428312742.

Sea ice concentration data from 20 March 2022 to 10 April 2022 were obtained from <https://www.meereisportal.de> (grant: REKLIM-  
2013-04).

We thank Christof Lüpkes and Jörg Hartmann from the Alfred Wegener Institute (AWI) for providing Polar 6 noseboom air temperature  
595 measurements.

## References

- NASA Worldview, MODIS Terra, <https://worldview.earthdata.nasa.gov>.
- Avramov, A., Ackerman, A. S., Fridlind, A. M., van Dierenhoven, B., Botta, G., Aydin, K., Verlinde, J., Korolev, A. V., Strapp, J. W., McFarquhar, G. M., Jackson, R., Brooks, S. D., Glen, A., and Wolde, M.: Toward Ice Formation Closure in Arctic Mixed-Phase Boundary Layer Clouds during ISDAC, *Journal of Geophysical Research: Atmospheres*, 116, <https://doi.org/10.1029/2011JD015910>, 2011.
- 600 Baumgardner, D., Brenguier, J. L., Bucholtz, A., Coe, H., DeMott, P., Garrett, T. J., Gayet, J. F., Hermann, M., Heymsfield, A., Korolev, A., Krämer, M., Petzold, A., Strapp, W., Pilewskie, P., Taylor, J., Twohy, C., Wendisch, M., Bachalo, W., and Chuang, P.: Airborne Instruments to Measure Atmospheric Aerosol Particles, Clouds and Radiation: A Cook's Tour of Mature and Emerging Technology, *Atmospheric Research*, 102, 10–29, <https://doi.org/10.1016/j.atmosres.2011.06.021>, 2011.
- 605 Blanke, A., Heymsfield, A. J., Moser, M., and Trömel, S.: Evaluation of polarimetric ice microphysical retrievals with OLYMPEX campaign data, *Atmospheric Measurement Techniques*, 16, 2089–2106, <https://doi.org/10.5194/amt-16-2089-2023>, 2023.
- Chase, R. J., Finlon, J. A., Borque, P., McFarquhar, G. M., Nesbitt, S. W., Tanelli, S., Sy, O. O., Durden, S. L., and Poellot, M. R.: Evaluation of Triple-Frequency Radar Retrieval of Snowfall Properties Using Coincident Airborne In Situ Observations During OLYMPEX, *Geophysical Research Letters*, 45, 5752–5760, <https://doi.org/10.1029/2018GL077997>, 2018.
- 610 Crosier, J., Bower, K. N., Choulaton, T. W., Westbrook, C. D., Connolly, P. J., Cui, Z. Q., Crawford, I. P., Capes, G. L., Coe, H., Dorsey, J. R., Williams, P. I., Illingworth, A. J., Gallagher, M. W., and Blyth, A. M.: Observations of Ice Multiplication in a Weakly Convective Cell Embedded in Supercooled Mid-Level Stratus, *Atmospheric Chemistry and Physics*, 11, 257–273, <https://doi.org/10.5194/acp-11-257-2011>, 2011.
- Ehrlich, A., Wendisch, M., Lüpkes, C., Buschmann, M., Bozem, H., Chechin, D., Clemen, H.-C., Dupuy, R., Eppers, O., Hartmann, J., Herber, A., Jäkel, E., Järvinen, E., Jourdan, O., Kästner, U., Kliensch, L.-L., Köllner, F., Mech, M., Mertes, S., Neuber, R., Ruiz-Donoso, E., Schnaiter, M., Schneider, J., Stapf, J., and Zanatta, M.: A Comprehensive in Situ and Remote Sensing Data Set from the Arctic CLOUD Observations Using Airborne Measurements during Polar Day (ACLOUD) Campaign, *Earth System Science Data*, 11, 1853–1881, <https://doi.org/10.5194/essd-11-1853-2019>, 2019.
- 615 Erfani, E. and Mitchell, D. L.: Growth of Ice Particle Mass and Projected Area during Riming, *Atmospheric Chemistry and Physics*, 17, 1241–1257, <https://doi.org/10.5194/acp-17-1241-2017>, 2017.
- Field, P. R., Heymsfield, A. J., and Bansemer, A.: Shattering and Particle Interarrival Times Measured by Optical Array Probes in Ice Clouds, *Journal of Atmospheric and Oceanic Technology*, 23, 1357–1371, <https://doi.org/10.1175/JTECH1922.1>, 2006.
- Fitch, K. E. and Garrett, T. J.: Graupel Precipitating From Thin Arctic Clouds With Liquid Water Paths Less Than 50 g M<sup>-2</sup>, *Geophysical Research Letters*, 49, e2021GL094 075, <https://doi.org/10.1029/2021GL094075>, 2022.
- 625 Garrett, T. J. and Yuter, S. E.: Observed Influence of Riming, Temperature, and Turbulence on the Fallspeed of Solid Precipitation, *Geophysical Research Letters*, 41, 6515–6522, <https://doi.org/10.1002/2014GL061016>, 2014.
- Gergely, M., Cooper, S. J., and Garrett, T. J.: Using Snowflake Surface-Area-to-Volume Ratio to Model and Interpret Snowfall Triple-Frequency Radar Signatures, *Atmospheric Chemistry and Physics*, 17, 12 011–12 030, <https://doi.org/10.5194/acp-17-12011-2017>, 2017.
- Gierens, R., Kneifel, S., Shupe, M. D., Ebell, K., Maturilli, M., and Löhnert, U.: Low-Level Mixed-Phase Clouds in a Complex Arctic Environment, *Atmospheric Chemistry and Physics*, 20, 3459–3481, <https://doi.org/10.5194/acp-20-3459-2020>, 2020.
- 630 Harimaya, T. and Sato, M.: Measurement of the Riming Amount on Snowflakes, *Journal of the Faculty of Science, Hokkaido University*, 8, 355–366, 1989.

- Heymsfield, A. J.: A Comparative Study of the Rates of Development of Potential Graupel and Hail Embryos in High Plains Storms, *Journal of the Atmospheric Sciences*, 39, 2867–2897, [https://doi.org/10.1175/1520-0469\(1982\)039<2867:ACSOTR>2.0.CO;2](https://doi.org/10.1175/1520-0469(1982)039<2867:ACSOTR>2.0.CO;2), 1982.
- 635 Hogan, R. J. and Westbrook, C. D.: Equation for the Microwave Backscatter Cross Section of Aggregate Snowflakes Using the Self-Similar Rayleigh–Gans Approximation, *Journal of the Atmospheric Sciences*, 71, 3292–3301, <https://doi.org/10.1175/JAS-D-13-0347.1>, 2014.
- Hogan, R. J., Honeyager, R., Tyynelä, J., and Kneifel, S.: Calculating the Millimetre-Wave Scattering Phase Function of Snowflakes Using the Self-Similar Rayleigh–Gans Approximation, *Quarterly Journal of the Royal Meteorological Society*, 143, 834–844, <https://doi.org/10.1002/qj.2968>, 2017.
- 640 Intrieri, J. M. and Shupe, M. D.: Characteristics and Radiative Effects of Diamond Dust over the Western Arctic Ocean Region, *Journal of Climate*, 17, 2953–2960, [https://doi.org/10.1175/1520-0442\(2004\)017<2953:CAREOD>2.0.CO;2](https://doi.org/10.1175/1520-0442(2004)017<2953:CAREOD>2.0.CO;2), 2004.
- Kay, J. E. and L’Ecuyer, T.: Observational Constraints on Arctic Ocean Clouds and Radiative Fluxes during the Early 21st Century, *Journal of Geophysical Research: Atmospheres*, 118, 7219–7236, <https://doi.org/10.1002/jgrd.50489>, 2013.
- Kneifel, S. and Moisseev, D.: Long-Term Statistics of Riming in Nonconvective Clouds Derived from Ground-Based Doppler Cloud Radar  
645 Observations, *Journal of the Atmospheric Sciences*, 77, 3495–3508, <https://doi.org/10.1175/JAS-D-20-0007.1>, 2020.
- Korolev, A., McFarquhar, G., Field, P. R., Franklin, C., Lawson, P., Wang, Z., Williams, E., Abel, S. J., Axisa, D., Borrmann, S., Crosier, J., Fugal, J., Krämer, M., Lohmann, U., Schlenczek, O., Schnaiter, M., and Wendisch, M.: Mixed-Phase Clouds: Progress and Challenges, *Meteorological Monographs*, 58, 5.1–5.50, <https://doi.org/10.1175/AMSMONOGRAPHS-D-17-0001.1>, 2017.
- Korolev, A. V., Strapp, J. W., Isaac, G. A., and Nevzorov, A. N.: The Nevzorov Airborne Hot-Wire LWC–TWC Probe: Principle of Oper-  
650 ation and Performance Characteristics, *Journal of Atmospheric and Oceanic Technology*, 15, 1495–1510, [https://doi.org/10.1175/1520-0426\(1998\)015<1495:TNAHWL>2.0.CO;2](https://doi.org/10.1175/1520-0426(1998)015<1495:TNAHWL>2.0.CO;2), 1998.
- Lance, S., Brock, C. A., Rogers, D., and Gordon, J. A.: Water Droplet Calibration of the Cloud Droplet Probe (CDP) and in-Flight Performance in Liquid, Ice and Mixed-Phase Clouds during ARCPAC, *Atmospheric Measurement Techniques*, 3, 1683–1706, <https://doi.org/10.5194/amt-3-1683-2010>, 2010.
- 655 Leinonen, J. and Moisseev, D.: What Do Triple-Frequency Radar Signatures Reveal about Aggregate Snowflakes?, *Journal of Geophysical Research: Atmospheres*, 120, 229–239, <https://doi.org/10.1002/2014JD022072>, 2015.
- Leinonen, J. and Szyrmer, W.: Radar Signatures of Snowflake Riming: A Modeling Study, *Earth and Space Science*, 2, 346–358, <https://doi.org/10.1002/2015EA000102>, 2015.
- Leinonen, J., Moisseev, D., and Nousiainen, T.: Linking Snowflake Microstructure to Multi-Frequency Radar Observations, *Journal of Geo-  
660 physical Research: Atmospheres*, 118, 3259–3270, <https://doi.org/10.1002/jgrd.50163>, 2013.
- Lucke, J., Jurkat-Witschas, T., Heller, R., Hahn, V., Hamman, M., Breitfuss, W., Bora, V. R., Moser, M., and Voigt, C.: Icing wind tunnel measurements of supercooled large droplets using the 12 mm total water content cone of the Nevzorov probe, *Atmospheric Measurement Techniques*, 15, 7375–7394, 2022.
- Maahn, M., Löhnert, U., Kollias, P., Jackson, R. C., and McFarquhar, G. M.: Developing and Evaluating Ice Cloud Parameterizations for  
665 Forward Modeling of Radar Moments Using in Situ Aircraft Observations, *Journal of Atmospheric and Oceanic Technology*, 32, 880–903, <https://doi.org/10.1175/JTECH-D-14-00112.1>, 2015.
- Maahn, M., Turner, D. D., Löhnert, U., Posselt, D. J., Ebell, K., Mace, G. G., and Comstock, J. M.: Optimal Estimation Retrievals and Their Uncertainties: What Every Atmospheric Scientist Should Know, *Bulletin of the American Meteorological Society*, 101, E1512–E1523, <https://doi.org/10.1175/BAMS-D-19-0027.1>, 2020.

- 670 Maherndl, N., Maahn, M., Tridon, F., Leinonen, J., Ori, D., and Kneifel, S.: A riming-dependent parameterization of scattering by snowflakes using the self-similar Rayleigh–Gans Approximation, *Quarterly Journal of the Royal Meteorological Society*, n/a, <https://doi.org/https://doi.org/10.1002/qj.4573>, 2023a.
- Maherndl, N., Maahn, M., Tridon, F., Leinonen, J., Ori, D., and Kneifel, S.: Data set of simulated rimed aggregates for "A riming-dependent parameterization of scattering by snowflakes using the self-similar Rayleigh-Gans approximation", <https://doi.org/10.5281/zenodo.7757034>, 2023b.
- 675 Mason, S. L., Chiu, C. J., Hogan, R. J., Moisseev, D., and Kneifel, S.: Retrievals of Riming and Snow Density From Vertically Pointing Doppler Radars, *Journal of Geophysical Research: Atmospheres*, 123, 13,807–13,834, <https://doi.org/10.1029/2018JD028603>, 2018.
- McFarquhar, G. M., Zhang, G., Poellot, M. R., Kok, G. L., McCoy, R., Tooman, T., Fridlind, A., and Heymsfield, A. J.: Ice Properties of Single-Layer Stratocumulus during the Mixed-Phase Arctic Cloud Experiment: 1. Observations, *Journal of Geophysical Research: Atmospheres*, 112, <https://doi.org/10.1029/2007JD008633>, 2007.
- 680 Mech, M., Kliesch, L.-L., Anhäuser, A., Rose, T., Kollias, P., and Crewell, S.: Microwave Radar/Radiometer for Arctic Clouds (MiRAC): First Insights from the ALOUD Campaign, *Atmospheric Measurement Techniques*, 12, 5019–5037, <https://doi.org/10.5194/amt-12-5019-2019>, 2019.
- Mech, M., Maahn, M., Kneifel, S., Ori, D., Orlandi, E., Kollias, P., Schemann, V., and Crewell, S.: PAMTRA 1.0: The Passive and Active Microwave Radiative TRANSfer Tool for Simulating Radiometer and Radar Measurements of the Cloudy Atmosphere, *Geoscientific Model Development*, 13, 4229–4251, <https://doi.org/10.5194/gmd-13-4229-2020>, 2020.
- 685 Mech, M., Ehrlich, A., Herber, A., Lüpkes, C., Wendisch, M., Becker, S., Boose, Y., Chechin, D., Crewell, S., Dupuy, R., Gourbeyre, C., Hartmann, J., Jäkel, E., Jourdan, O., Kliesch, L.-L., Klingebiel, M., Kulla, B. S., Mioche, G., Moser, M., Risse, N., Ruiz-Donoso, E., Schäfer, M., Stapf, J., and Voigt, C.: MOSAiC-ACA and AFLUX - Arctic Airborne Campaigns Characterizing the Exit Area of MOSAiC, *Scientific Data*, 9, 790, <https://doi.org/10.1038/s41597-022-01900-7>, 2022a.
- 690 Mech, M., Risse, N., Marrollo, G., and Paul, D.: ac3airborne, <https://doi.org/10.5281/zenodo.7305586>, 2022b.
- Mie, G.: Beiträge Zur Optik Trüber Medien, Speziell Kolloidaler Metallösungen, *Annalen der Physik*, 330, 377–445, <https://doi.org/10.1002/andp.19083300302>, 1908.
- Mitchell, D. L.: Use of Mass- and Area-Dimensional Power Laws for Determining Precipitation Particle Terminal Velocities, *Journal of the Atmospheric Sciences*, 53, 1710–1723, [https://doi.org/10.1175/1520-0469\(1996\)053<1710:UOMAAD>2.0.CO;2](https://doi.org/10.1175/1520-0469(1996)053<1710:UOMAAD>2.0.CO;2), 1996.
- 695 Moisseev, D., von Lerber, A., and Tiira, J.: Quantifying the Effect of Riming on Snowfall Using Ground-Based Observations, *Journal of Geophysical Research: Atmospheres*, 122, 4019–4037, <https://doi.org/10.1002/2016JD026272>, 2017.
- Morrison, H., de Boer, G., Feingold, G., Harrington, J., Shupe, M. D., and Sulia, K.: Resilience of Persistent Arctic Mixed-Phase Clouds, *Nature Geoscience*, 5, 11–17, <https://doi.org/10.1038/ngeo1332>, 2012.
- 700 Morrison, H., van Lieer-Walqui, M., Fridlind, A. M., Grabowski, W. W., Harrington, J. Y., Hoose, C., Korolev, A., Kumjian, M. R., Milbrandt, J. A., Pawlowska, H., Posselt, D. J., Prat, O. P., Reimel, K. J., Shima, S.-I., van Diedenhoven, B., and Xue, L.: Confronting the Challenge of Modeling Cloud and Precipitation Microphysics, *Journal of Advances in Modeling Earth Systems*, 12, e2019MS001689, <https://doi.org/10.1029/2019MS001689>, 2020.
- Moser, M. and Voigt, C.: DLR in-situ cloud measurements during AFLUX Arctic airborne campaign, <https://doi.org/10.1594/PANGAEA.940564>, 2022.
- 705 Moser, M., Voigt, C., and Hahn, V.: DLR in-situ cloud measurements during MOSAiC-ACA Arctic airborne campaign, <https://doi.org/10.1594/PANGAEA.940557>, 2022.

- Moser, M., Voigt, C., Jurkat-Witschas, T., Hahn, V., Mioche, G., Jourdan, O., Dupuy, R., Gourbeyre, C., Schwarzenboeck, A., Lucke, J., Boose, Y., Mech, M., Borrmann, S., Ehrlich, A., Herber, A., Lüpkes, C., and Wendisch, M.: Microphysical and Thermodynamic Phase Analyses of Arctic Low-Level Clouds Measured above the Sea Ice and the Open Ocean in Spring and Summer, *Atmospheric Chemistry and Physics Discussions* [preprint], pp. 1–27, <https://doi.org/10.5194/acp-2023-44>, 2023.
- Mosimann, L.: An Improved Method for Determining the Degree of Snow Crystal Riming by Vertical Doppler Radar, *Atmospheric Research*, 37, 305–323, [https://doi.org/10.1016/0169-8095\(94\)00050-N](https://doi.org/10.1016/0169-8095(94)00050-N), 1995.
- Mosimann, L., Weingartner, E., and Waldvogel, A.: An Analysis of Accreted Drop Sizes and Mass on Rimed Snow Crystals, *Journal of the Atmospheric Sciences*, 51, 1548–1558, [https://doi.org/10.1175/1520-0469\(1994\)051<1548:AAOADS>2.0.CO;2](https://doi.org/10.1175/1520-0469(1994)051<1548:AAOADS>2.0.CO;2), 1994.
- Müller, G., Brümmer, B., and Alpers, W.: Roll Convection within an Arctic Cold-Air Outbreak: Interpretation of In Situ Aircraft Measurements and Spaceborne SAR Imagery by a Three-Dimensional Atmospheric Model, *Monthly Weather Review*, 127, 363–380, [https://doi.org/10.1175/1520-0493\(1999\)127<0363:RCWAAC>2.0.CO;2](https://doi.org/10.1175/1520-0493(1999)127<0363:RCWAAC>2.0.CO;2), 1999.
- Nguyen, C. M., Wolde, M., Battaglia, A., Nichman, L., Bliankinshtein, N., Haimov, S., Bala, K., and Schuettemeyer, D.: Coincident in Situ and Triple-Frequency Radar Airborne Observations in the Arctic, *Atmospheric Measurement Techniques*, 15, 775–795, <https://doi.org/10.5194/amt-15-775-2022>, 2022.
- Ori, D., von Terzi, L., Karrer, M., and Kneifel, S.: snowScatt 1.0: Consistent Model of Microphysical and Scattering Properties of Rimed and Unrimed Snowflakes Based on the Self-Similar Rayleigh–Gans Approximation, *Geoscientific Model Development*, 14, 1511–1531, <https://doi.org/10.5194/gmd-14-1511-2021>, 2021.
- Oue, M., Galletti, M., Verlinde, J., Ryzhkov, A., and Lu, Y.: Use of X-Band Differential Reflectivity Measurements to Study Shallow Arctic Mixed-Phase Clouds, *Journal of Applied Meteorology and Climatology*, 55, 403–424, <https://doi.org/10.1175/JAMC-D-15-0168.1>, 2016.
- Praz, C., Roulet, Y.-A., and Berne, A.: Solid Hydrometeor Classification and Riming Degree Estimation from Pictures Collected with a Multi-Angle Snowflake Camera, *Atmospheric Measurement Techniques*, 10, 1335–1357, <https://doi.org/10.5194/amt-10-1335-2017>, 2017.
- Rantanen, M., Karpechko, A. Y., Lipponen, A., Nordling, K., Hyvärinen, O., Ruosteenoja, K., Vihma, T., and Laaksonen, A.: The Arctic Has Warmed Nearly Four Times Faster than the Globe since 1979, *Communications Earth & Environment*, 3, 1–10, <https://doi.org/10.1038/s43247-022-00498-3>, 2022.
- Rodgers, C. D.: *Inverse Methods for Atmospheric Sounding: Theory and Practice*, World Scientific, <https://doi.org/10.1142/3171>, 2000.
- Rosenkranz, P. W.: Water vapor microwave continuum absorption: A comparison of measurements and models, *Radio Sci.*, 33, 919–928, 1998.
- Ruiz-Donoso, E., Ehrlich, A., Schäfer, M., Jäkel, E., Schemann, V., Crewell, S., Mech, M., Kulla, B. S., Kliesch, L.-L., Neuber, R., and Wendisch, M.: Small-scale structure of thermodynamic phase in Arctic mixed-phase clouds observed by airborne remote sensing during a cold air outbreak and a warm air advection event, *Atmospheric Chemistry and Physics*, 20, 5487–5511, <https://doi.org/10.5194/acp-20-5487-2020>, 2020.
- Seifert, A., Leinonen, J., Siewert, C., and Kneifel, S.: The Geometry of Rimed Aggregate Snowflakes: A Modeling Study, *Journal of Advances in Modeling Earth Systems*, 11, 712–731, <https://doi.org/10.1029/2018MS001519>, 2019.
- Shupe, M. D.: Clouds at Arctic Atmospheric Observatories. Part II: Thermodynamic Phase Characteristics, *Journal of Applied Meteorology and Climatology*, 50, 645–661, <https://doi.org/10.1175/2010JAMC2468.1>, 2011.
- Shupe, M. D. and Intrieri, J. M.: Cloud Radiative Forcing of the Arctic Surface: The Influence of Cloud Properties, Surface Albedo, and Solar Zenith Angle, *Journal of Climate*, 17, 616–628, [https://doi.org/10.1175/1520-0442\(2004\)017<0616:CRFOTA>2.0.CO;2](https://doi.org/10.1175/1520-0442(2004)017<0616:CRFOTA>2.0.CO;2), 2004.



- 745 Shupe, M. D., Matrosov, S. Y., and Uttal, T.: Arctic Mixed-Phase Cloud Properties Derived from Surface-Based Sensors at SHEBA, *Journal of the Atmospheric Sciences*, 63, 697–711, <https://doi.org/10.1175/JAS3659.1>, 2006.
- Stachlewska, I. S., Neuber, R., Lampert, A., Ritter, C., and Wehrle, G.: AMALi – the Airborne Mobile Aerosol Lidar for Arctic Research, *Atmospheric Chemistry and Physics*, 10, 2947–2963, <https://doi.org/10.5194/acp-10-2947-2010>, 2010.
- Takahashi, T.: Influence of Liquid Water Content and Temperature on the Form and Growth of Branched Planar Snow Crystals in a Cloud, *Journal of the Atmospheric Sciences*, 71, 4127–4142, <https://doi.org/10.1175/JAS-D-14-0043.1>, 2014.
- 750 Takahashi, T., Endoh, T., Wakahama, G., and Fukuta, N.: Vapor Diffusional Growth of Free-Falling Snow Crystals between -3 and -23°C, *Journal of the Meteorological Society of Japan. Ser. II*, 69, 15–30, [https://doi.org/10.2151/jmsj1965.69.1\\_15](https://doi.org/10.2151/jmsj1965.69.1_15), 1991.
- Tian, J., Dong, X., Xi, B., Wang, J., Homeyer, C. R., McFarquhar, G. M., and Fan, J.: Retrievals of ice cloud microphysical properties of deep convective systems using radar measurements, *Journal of Geophysical Research: Atmospheres*, 121, <https://doi.org/10.1002/2015jd024686>, 2016.
- 755 Trömel, S., Simmer, C., Blahak, U., Blanke, A., Doktorowski, S., Ewald, F., Frech, M., Gergely, M., Hagen, M., Janjic, T., Kalesse-Los, H., Kneifel, S., Knote, C., Mendrok, J., Moser, M., Köcher, G., Mühlbauer, K., Myagkov, A., Pejčic, V., Seifert, P., Shrestha, P., Teisseire, A., von Terzi, L., Tetoni, E., Vogl, T., Voigt, C., Zeng, Y., Zinner, T., and Quaas, J.: Overview: Fusion of radar polarimetry and numerical atmospheric modelling towards an improved understanding of cloud and precipitation processes, *Atmospheric Chemistry and Physics*, 21, 17291–17314, <https://doi.org/10.5194/acp-21-17291-2021>, 2021.
- 760 Vogl, T., Maahn, M., Kneifel, S., Schimmel, W., Moisseev, D., and Kalesse-Los, H.: Using Artificial Neural Networks to Predict Riming from Doppler Cloud Radar Observations, *Atmospheric Measurement Techniques*, 15, 365–381, <https://doi.org/10.5194/amt-15-365-2022>, 2022.
- Waltz, F., Schnaiter, M., Leisner, T., and Järvinen, E.: In Situ Observation of Riming in Mixed-Phase Clouds Using the PHIPS Probe, *Atmospheric Chemistry and Physics*, 22, 7087–7103, <https://doi.org/10.5194/acp-22-7087-2022>, 2022.
- 765 Walbröl, A., Michaelis, J., Becker, S., Dorff, H., Gorodetskaya, I., Kirbus, B., Lauer, M., Maherndl, N., Maturilli, M., Mayer, J., Müller, H., Neggens, R. A. J., Paulus, F. M., Röttenbacher, J., Rückert, J. E., Schirmacher, I., Slättberg, N., Ehrlich, A., Wendisch, M., and Crewell, S.: Environmental conditions in the North Atlantic sector of the Arctic during the HALO-(AC)<sup>3</sup> campaign, *EGU sphere*, 2023, 1–48, <https://doi.org/10.5194/egusphere-2023-668>, 2023.
- 770 Wendisch, M., Keil, A., and Korolev, A. V.: FSSP Characterization with Monodisperse Water Droplets, *Journal of Atmospheric and Oceanic Technology*, 13, 1152–1165, [https://doi.org/10.1175/1520-0426\(1996\)013<1152:FCWMWD>2.0.CO;2](https://doi.org/10.1175/1520-0426(1996)013<1152:FCWMWD>2.0.CO;2), 1996.
- Wendisch, M., Macke, A., Ehrlich, A., Lüpkes, C., Mech, M., Chechin, D., Dethloff, K., Velasco, C. B., Bozem, H., Brückner, M., Clemen, H.-C., Crewell, S., Donth, T., Dupuy, R., Ebell, K., Egerer, U., Engelmann, R., Engler, C., Eppers, O., Gehrman, M., Gong, X., Gottschalk, M., Gourbeyre, C., Griesche, H., Hartmann, J., Hartmann, M., Heinold, B., Herber, A., Herrmann, H., Heygster, G., Hoor, P., Jafariserajehlou, S., Jäkel, E., Järvinen, E., Jourdan, O., Kästner, U., Kecorius, S., Knudsen, E. M., Köllner, F., Kretzschmar, J., Lelli, L., Leroy, D., Maturilli, M., Mei, L., Mertes, S., Mioche, G., Neuber, R., Nicolaus, M., Nomokonova, T., Notholt, J., Palm, M., van Pinxteren, M., Quaas, J., Richter, P., Ruiz-Donoso, E., Schäfer, M., Schmieder, K., Schnaiter, M., Schneider, J., Schwarzenböck, A., Seifert, P., Shupe, M. D., Siebert, H., Spreen, G., Stapf, J., Stratmann, F., Vogl, T., Welti, A., Wex, H., Wiedensohler, A., Zanatta, M., and Zeppenfeld, S.: The Arctic Cloud Puzzle: Using ALOUD/PASCAL Multiplatform Observations to Unravel the Role of Clouds and Aerosol Particles in Arctic Amplification, *Bulletin of the American Meteorological Society*, 100, 841–871, <https://doi.org/10.1175/BAMS-D-18-0072.1>, 2019.

- Wendisch, M., Brückner, M., Crewell, S., Ehrlich, A., Notholt, J., Lüpkes, C., Macke, A., Burrows, J. P., Rinke, A., Quaas, J., Maturilli, M., Schemann, V., Shupe, M. D., Akansu, E. F., Barrientos-Velasco, C., Bärfuss, K., Blechschmidt, A.-M., Block, K., Bougoudis, I., Bozem, H., Böckmann, C., Bracher, A., Bresson, H., Bretschneider, L., Buschmann, M., Chechin, D. G., Chylik, J., Dahlke, S., Deneke, H., Dethloff, K., Donth, T., Dorn, W., Dupuy, R., Ebell, K., Egerer, U., Engelmann, R., Eppers, O., Gerdes, R., Gierens, R., Gorodetskaya, I. V., Gottschalk, M., Griesche, H., Gryanik, V. M., Handorf, D., Harm-Altstädter, B., Hartmann, J., Hartmann, M., Heinold, B., Herber, A., Herrmann, H., Heygster, G., Höschel, I., Hofmann, Z., Hölemann, J., Hünerbein, A., Jafariserajehlou, S., Jäkel, E., Jacobi, C., Janout, M., Jansen, F., Jourdan, O., Jurányi, Z., Kalesse-Los, H., Kanzow, T., Käthner, R., Kliesch, L. L., Klingebiel, M., Knudsen, E. M., Kovács, T., Körtke, W., Krampe, D., Kretzschmar, J., Kreyling, D., Kulla, B., Kunkel, D., Lampert, A., Lauer, M., Lelli, L., von Lerber, A., Linke, O., Löhnert, U., Lonardi, M., Losa, S. N., Losch, M., Maahn, M., Mech, M., Mei, L., Mertes, S., Metzner, E., Mewes, D., Michaelis, J., Mioche, G., Moser, M., Nakoudi, K., Neggers, R., Neuber, R., Nomokonova, T., Oelker, J., Papakonstantinou-Presvelou, I., Pätzold, F., Pefanis, V., Pohl, C., van Pinxteren, M., Radovan, A., Rhein, M., Rex, M., Richter, A., Risse, N., Ritter, C., Rostosky, P., Rozanov, V. V., Donoso, E. R., Garfias, P. S., Salzmann, M., Schacht, J., Schäfer, M., Schneider, J., Schnierstein, N., Seifert, P., Seo, S., Siebert, H., Soppa, M. A., Spreen, G., Stachlewska, I. S., Stapf, J., Stratmann, F., Tegen, I., Viceto, C., Voigt, C., Vountas, M., Walbröl, A., Walter, M., Wehner, B., Wex, H., Willmes, S., Zanatta, M., and Zeppenfeld, S.: Atmospheric and Surface Processes, and Feedback Mechanisms Determining Arctic Amplification: A Review of First Results and Prospects of the (AC)<sup>3</sup> Project, *Bulletin of the American Meteorological Society*, 104, E208 – E242, <https://doi.org/https://doi.org/10.1175/BAMS-D-21-0218.1>, 2023.
- Wendisch, M. et al.: Quasi-Lagrange airborne observations of air mass transports into and out of the Arctic: Overview of the HALO—(AC)<sup>3</sup> campaign [in prep.], 2023.
- Wesche, C., Steinhage, D., and Nixdorf, U.: Polar Aircraft Polar5 and Polar6 Operated by the Alfred Wegener Institute, *Journal of large-scale research facilities JLSRF*, 2, A87–A87, <https://doi.org/10.17815/jlsrf-2-153>, 2016.
- Wolde, M., Korolev, A., Schüttemeyer, D., Baibakov, K., Barker, H., Bastian, M., Battaglia, A., Blanchet, J., Haimov, S., Heckman, I., Hudak, D., Mariani, Z., Michelson, D., Nguyen, C., Nichman, L., , and Rodriguez, P.: Radar Snow Experiment for future precipitation mission (RadSnowExp), *Living Planet Symposium*, Milan, Italia, 13–17 May, 2019.
- Yang, F., Ovchinnikov, M., and Shaw, R. A.: Minimalist Model of Ice Microphysics in Mixed-Phase Stratiform Clouds, *Geophysical Research Letters*, 40, 3756–3760, <https://doi.org/10.1002/grl.50700>, 2013.
- Zuidema, P., Baker, B., Han, Y., Intrieri, J., Key, J., Lawson, P., Matrosov, S., Shupe, M., Stone, R., and Uttal, T.: An Arctic Springtime Mixed-Phase Cloudy Boundary Layer Observed during SHEBA, *Journal of the Atmospheric Sciences*, 62, 160–176, <https://doi.org/10.1175/JAS-3368.1>, 2005.